

Czech technical university in Prague
Faculty of Nuclear Sciences and Physical Engineering

Department of Physics

Field: Experimental Nuclear and Particle Physics



Electromagnetic processes at STAR experiment with regard of colliding beam dynamics

BACHELOR THESIS

Author: Dominik Šmíd
Supervisor: Ing. Jaroslav Adam, Ph.D.
Year: 2024

České vysoké učení technické v Praze
Fakulta jaderná a fyzikálně inženýrská

Katedra fyziky

Obor: Experimentální jaderná a částicová fyzika



Elektromagnetické procesy na experimentu STAR s ohledem na dynamiku vstřícných svazků

BAKALÁŘSKÁ PRÁCE

Vypracoval: Dominik Šmíd
Vedoucí práce: Ing. Jaroslav Adam, Ph.D.
Rok: 2024

ZADÁNÍ BAKALÁŘSKÉ PRÁCE

Akademický rok: 2022/2023



Student: Dominik Šmíd

Studijní program: Aplikace přírodních věd

Obor: Experimentální jaderná a částicová fyzika

Název práce: Elektromagnetické procesy na experimentu STAR s ohledem na
(česky) dynamiku vstřícných svazků

Název práce: Electromagnetic processes at STAR experiment with regard of colliding
(anglicky) beam dynamics

Jazyk práce: angličtina

Pokyny pro vypracování:

Srážky těžkých iontů nabízejí řadu možností ke studiu základních elektromagnetických interakcí fotonů na fotonech nebo fotonů na jádrech. Takové interakce se dějí za vysokých energií a za přesně definovaných experimentálních podmínek. V rámci bakalářské práce student přispěje k analýze ultra-periferálních srážek (experimentální nástroj pro navození elektromagnetických interakcí) s ohledem na dynamiku srážejících se svazků, a to v následujících bodech:

- 1) prostuduje základní principy ultra-periferálních srážek a konstrukci experimentu STAR a urychlovače RHIC
- 2) v rámci technických možností reprodukuje pozorování částice J/ψ v ultra-periferálních AuAu srážkách
- 3) provede studium specifické struktury interakčních bodů podél osy svazku v AuAu ultra-periferálních srážkách
- 4) porovná specifickou strukturu z předchozího bodu s výsledky simulace dynamiky vstřícných svazků

Doporučená literatura:

- [1] S. Klein, J. Nystrand: Ultraperipheral nuclear collisions, Phys.Today 70 (2017) 10, 40-47
[2] J.G. Contreras, J.D. Tapia Takaki: Ultra-peripheral heavy-ion collisions at the LHC, Int.J.Mod.Phys.A 30 (2015) 1542012
[3] J. Adam: Coherent J/ψ photoproduction in ultra-peripheral collisions at STAR, PoS DIS2019 (2019) 042

Jméno a pracoviště vedoucího bakalářské práce:

Ing. Jaroslav Adam, Ph.D.

Katedra fyziky, Fakulta jaderná a fyzikálně inženýrská ČVUT v Praze

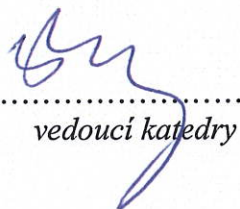
Datum zadání bakalářské práce: 20.10.2022

Termín odevzdání bakalářské práce: 02.08.2023

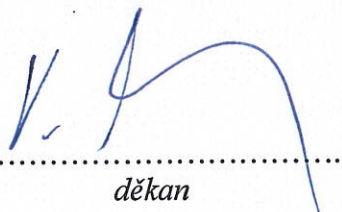
Doba platnosti zadání je dva roky od data zadání.



garant oboru



vedoucí katedry



děkan

V Praze dne 20.10.2022

ČESKÉ VYSOKÉ UČENÍ TECHNICKÉ
V PRAZE

Fakulta jaderná a fyzikálně inženýrská

Břehová 7
115 19 Praha 1



PROHLÁŠENÍ

Já, níže podepsaný

Jméno a příjmení studenta: Dominik Šmíd

Osobní číslo: 486410

Název studijního programu (oboru): Experimentální jaderná a částicová fyzika

prohlašuji, že jsem bakalářskou práci s názvem:

Elektromagnetické procesy na experimentu STAR s ohledem na dynamiku vstřícných svazků

vypracoval samostatně a uvedl veškeré použité informační zdroje v souladu s Metodickým pokynem o dodržování etických principů při přípravě vysokoškolských závěrečných prací.

V Praze dne 8.1.2024

.....
podpis

Acknowledgement

I am very grateful to my supervisor Ing. Jaroslav Adam, Ph.D. for his patience, willingness, and professional assistance during writing this thesis and for providing valuable professional information for processing the final chapter. I would also like to express my gratitude to my family and friends who supported me during my studies and writing this thesis.

Dominik Šmíd

Thesis title:

Electromagnetic processes at STAR experiment with regard of colliding beam dynamics

Author: Dominik Šmíd

Programme: Application of Natural Sciences

Field of study: Experimental Nuclear and Particle Physics

Type of thesis: Bachelor thesis

Supervisor: Ing. Jaroslav Adam, Ph.D

Department of Physics, Faculty of Nuclear Sciences and Physical Engineering, Czech Technical University in Prague

Abstract: The physics of ultra-peripheral collisions, which occur at large distances of colliding nuclei, enables a number of possibilities for investigating electromagnetic interactions of colliding particles. Collisions take place at high energies and under precisely defined experimental conditions, where the interaction of colliding nuclei, protons or collisions of protons with heavy nuclei can be observed. The study of ultra-peripheral collisions of heavy nuclei also provides an insight into the properties of the quark-gluon plasma, i.e. the state of matter under extreme conditions of high densities and temperatures, which correspond to the state of the universe shortly after its creation after the Big Bang. The physics of ultra-peripheral collisions is discussed in the first chapter of this work. The particle accelerators enabling the discussed type of collisions include the LHC at CERN or the RHIC at BNL. The second chapter of this work is devoted to the STAR experiment at RHIC, from which data for the analysis of the observation of the J/ψ particle and the specific structure of the interaction points along the beam axis originated, the results of which are discussed in the last chapter.

Key words: J/ψ photoproduction, heavy ion collisions, ultra-peripheral collisions, STAR experiment, interaction points

Název práce:

Elektromagnetické procesy na experimentu STAR s ohledem na dynamiku vstřícných svazků

Autor: Dominik Šmíd

Studijní program: Aplikace přírodních věd

Obor: Experimentální jaderná a částicová fyzika

Druh práce: Bakalářská práce

Vedoucí práce: Ing. Jaroslav Adam, Ph.D

Katedra fyziky, Fakulta jaderná a fyzikálně inženýrská, České vysoké učení technické v Praze

Abstrakt: Fyzika ultra periferálních srážek, ke kterým dochází na velkých vzdálenostech srážejících se jader, umožňuje řadu možností zkoumání elektromagnetických interakcí srážejících se částic. Srážky se dějí při vysokých energiích a za přesně definovaných experimentálních podmínkách, kdy lze pozorovat interakci srážejících se jader, protonů či srážky protonů s těžkými jádry. Studium ultra periferálních srážek těžkých jader rovněž umožňuje náhled do vlastností kvark-gluonového plazma, tedy stavu hmoty za extrémních podmínek vysokých hustot a teplot, které odpovídají stavu vesmíru v krátké době po jeho vzniku po Velkém třesku. Fyzika ultra periferálních srážek je probrána v první kapitole této práce. Mezi urychlovače částic, umožňující probíraný typ srážek patří LHC v CERNu nebo RHIC v BNL. Druhá kapitola této práce je věnována experimentu STAR na RHICu, ze kterého pochází data pro analýzu pozorování částice J/ψ a specifické struktury interakčních bodů podél osy svazku, jejíž výsledky jsou probrány v poslední kapitole.

Klíčová slova: J/ψ fotoprodukce, srážky těžkých jader, ultra-periferální srážky, STAR experiment, interakční body

Contents

List of Figures	xix
Introduction	1
1 Principles of Ultra-peripheral collisions	3
1.1 Standard model	3
1.1.1 Quarks, leptons, and hadrons	4
1.1.2 Interactions	5
1.2 Ultra-peripheral collisions	7
1.3 Photon flux	8
1.4 Exclusive Particle Production	10
1.4.1 Interference in Exclusive Vector meson Production	12
1.4.2 Non-UPC	13
1.5 Inclusive Photoproduction	13
1.6 Photoproduction	14
1.6.1 Proton's gluon distribution	15
1.6.2 Photoproduction of J/ψ	15
1.7 Two-photon production	16
1.7.1 Free e^+e^- pairs production	17
1.7.2 Meson Production in Two-Photon interactions	17
2 Experiment STAR at RHIC	19
2.1 BNL	19
2.2 RHIC	20
2.2.1 Radio Frequency (RF) system	23
2.2.2 Detectors at RHIC	25
2.3 STAR experiment at RHIC	26
3 Observation of J/ψ in UPCs and structure of interaction points	35
3.1 Physical quantities for particle collisions description	35
3.2 Data analysis of J/ψ in Au+Au at $\sqrt{s} = 200$ GeV	38
3.2.1 Data format	38
3.2.2 Trigger requirement and data selection	39
3.2.3 Data processing for J/ψ	40
3.2.4 Position of ZDC vertex	44
3.2.5 Simulation of colliding beams dynamics	49
Conclusion	57

Contents	xvii
Bibliography	59
Appendix	63

List of Figures

1.1	Periodic table of particles and intermediate particles of interactions of SM[1].	4
1.2	UPC of two highly charged, fast-moving ions Z1, Z2[2].	8
1.3	One photon (left) and two-photon interaction (right) in heavy ion collision[2].	9
1.4	Prediction of $d\sigma/dt$ for J/ψ in Au-Au collision at RHIC[2].	11
1.5	The STAR collaboration observed interference in the production of mesons ρ^0 at transverse momentum p_T [3].	12
1.6	J/ψ cross section as a function of transverse momentum p_T [4].	16
2.1	BNL heavy-ion collider complex overview [5].	20
2.2	BNL accelerator complex layout[6].	22
2.3	RHIC geometry layout [6].	23
2.4	Perspective view of the STAR detector, with a cutaway for inner detector system[7].	26
2.5	Cutaway side view of the STAR detector as configured in 2001 [7].	27
2.6	Two side views on the structure of an MRPC module [8].	29
2.7	Measurement in TPC detector of energy-loss dE/dx (upper left figure), $1/\beta^2$ measurement in TOF detector(upper left figure) and improved electron identification by combining the TOF and TPC measurements (lower figure) [9].	29
2.8	BEMC module (left) with its cross section (right) [10].	30
2.9	ZDC modules installed on STAR experiment [11].	31
2.10	Location of the FCS at the west side of the STAR experiment and a three-dimensional CAD model of the FCS [12].	32
3.1	Mass of dielectron pair e^+e^-	40
3.2	Transverse momentum of dielectron pair e^+e^-	40
3.3	Tracks rapidity	41
3.4	Part of code to open the file and get the tree with data.	41
3.5	Filling a histogram with data.	41
3.6	Mass of dielectron pair e^+e^- after restriction.	42
3.7	Transverse momentum of dielectron pair e^+e^- after restriction.	42
3.8	Tracks rapidity after restriction.	43
3.9	Restrictions to data.	43
3.10	z-vertex distribution along the beam axis.	44

3.11	Part of code for used classes imported from ROOT, getting data from a dataset and determining bins (maximum, minimum, and bin size). . .	45
3.12	Code for fit to logarithmic scale of displaying data (first part), and for data input from the tree (second part).	45
3.13	z-vertex distribution along the beam axis.	46
3.14	Code for 5 Gaussians used to fit the data.	47
3.15	Code for creating a model and fitting the data.	47
3.16	z-vertex position distribution fitted by the model of Gaussians together with the distance values between peaks.	48
3.17	Two beams (Blue and Yellow) consisting of several bunches of particles in the collider with 3 selected bunches.	49
3.18	Two beams (Blue and Yellow) consisting of several bunches of particles in the collider with 3 selected bunches.	50
3.19	Close-up look at Bunch 1	51
3.20	Predicted vertex distribution for Bunch 1	51
3.21	Close-up look at Bunch 2	51
3.22	Predicted vertex distribution for Bunch 2	51
3.23	Close-up look at Bunch 3	51
3.24	Predicted vertex distribution for Bunch 3	51
3.25	Code for bunch rendering in a certain time interval.	52
3.26	Code for evolution.	52
3.27	Images from video for simulation of two opposing bundles of particles collision approximately 1 ns apart covering time interval (-5, 4) ns. . .	53
3.28	Images from video for simulation of overlap on the z-axis of two bunches in a time interval (-5, 4) ns.	54
3.29	Code for loading the data and functions for output.	63
3.30	Code for video creation.	64

Introduction

In high-energy physics, we can investigate the properties of nuclear matter at high energies, with a main interest in heavy ion collisions. Ultra peripheral collisions (UPC) are a type of collision that occurs at large distances at an impact parameter that is greater than the sum of the nuclear radii of the colliding particles in the presence of a strong electromagnetic field. These collisions take place outside the reach of the strong interaction, which is suppressed and collisions are governed by electromagnetic forces. Collisions of beams of heavy nuclei, protons, or collisions of protons with nuclei at particle accelerators at high energies under well-defined experimental conditions allow us to observe the interaction of electromagnetic fields from nuclei, which can be described as a photon flux, and thus the electromagnetic interaction of two photons or an interaction of photon and a nucleus.

The study of collisions of heavy nuclei also enables investigation and insight into the properties of quark-gluon plasma, i.e. the state of matter under extreme conditions of high densities and temperatures, which correspond to the state of the universe shortly after its creation after the Big Bang. During these collisions quarks and gluons, which are tightly bound in hadrons, are released and can move almost freely at small distances. Photoproduction at hadron colliders during UPCs of beams of proton and heavy nuclei, leading to the production of vector mesons can also serve as a tool for studying the internal structure of particles, investigated by quantum chromodynamics. Investigating the gluon distribution is possible due to the fact that photons couple weakly to charged particles and not to themselves and are suitable for studying the internal structure of protons and heavy nuclei. One of the particle accelerators on which heavy ion collisions can be studied is the Relativistic Heavy Ion Collider (RHIC) in Brookhaven National Laboratory (BNL), which allows collisions of mostly beams of gold nuclei at energies up to 200 GeV.

In the first chapter, the physics of UPCs during collisions of heavy nuclei, the result of which is the exclusive production of particles, is discussed in more detail. Specifically, the photoproduction of the J/ψ meson, which is measured at RHIC by its decay $J/\psi \rightarrow e^+e^-$. The first chapter also discusses the production of dilepton pairs from two-photon processes and the basic description and classification of particles within the framework of the Standard Model (SM).

The second chapter is focused on the accelerator complex at BNL, where its history and institutions are briefly mentioned. Part of this chapter consists of a description of the RHIC accelerator and the system used to capture and accelerate particles. In this chapter, a description of the experiments that are taking place at the accelerator or have taken place in the past is included. Emphasis is placed on

the description of the STAR experiment and the description of its individual parts.

In the third and last chapter, the physical quantities used in high-energy physics for particle collisions description are described at the beginning of the chapter, followed by the analysis of data from UPCs at the STAR experiment for Au+Au collisions at energies $\sqrt{s} = 200$ GeV. The first part of the analysis deals with the reproduction of the results of the observation of the J/ψ particle. The second part of the analysis is focused on investigating the specific structure of the distribution of the interaction points along the beam axis determined from the forward Zero Degree Calorimeters (ZDCs) detectors. The last part of this chapter discusses the created simulation of the collision of two opposing beams of Au+Au from run 14 covering the period from 25 March 2014 to 16 June 2014. The simulation was used for comparison of the structure of z-vertices and the time evolution of the interaction points during the collision.

Chapter 1

Principles of Ultra-peripheral collisions

Before starting the introduction to Ultra-peripheral collisions, which will be the main topic of this thesis, an introductory section of this chapter will be dedicated to the Standard Model and the primary classification and characterization of particles and interactions.

1.1 Standard model

The description and classification of the investigated particles and interactions are being done within the framework of the Standard Model (SM), which refers to the sum total of our knowledge of all the forces and particles. SM describes the interaction between particles as an interaction between quantum fields, the interaction is mediated and characterized by intermediate particles, which are force carriers. Interaction between two particles can therefore be described as an intermediate particle emitted by a field, by which the original interacting particle is replaced, and subsequently absorbed by the other field. Information for this section is based on [13],[14] and [15]

SM divides elementary particles based on their spin value into fermions with half-integer spin in units of Planck's constant \hbar , which are the elementary constituents of matter, and bosons with integer spin that govern a force. Figure 1.1 shows particles and force carriers. A different statistic is applied to each group of particles, Fermi-Dirac statistics apply to fermions and Bose-Einstein statistics apply to bosons. Each particle can be characterized by several quantities, and based on their values we can divide the particles into groups. These quantities are mass, electric charge, spin, lifetime, magnetic dipole moment, lepton and baryon number, strangeness, charm, beauty, and truth. The isospin and parity of the particle also influence the classification. [13]


















THREE GENERATIONS OF MATTER (FERMIONS)						INTERACTIONS/FORCE CARRIERS (BOSONS)	
QUARKS	Mass: 2.2 ⁺ Charge: 2/3 Spin: 1/2  Up	1,270 2/3 1/2  Charm	173,100 2/3 1/2  Top	GAUGE BOSONS (VECTOR BOSONS)	0 0 1  Gluon	SCALAR BOSONS	125,180 0 0  Higgs boson
	4.7 -1/3 1/2  Down	96 -1/3 1/2  Strange	4,180 -1/3 1/2  Bottom		0 0 1  Photon		
	0.511 -1 1/2  Electron	105.66 -1 1/2  Muon	1,776.8 -1 1/2  Tau		91,188 0 1  Z boson		
LEPTONS	<math><0.00000012</math> 0 1/2  Electron neutrino	<math><0.00000012</math> 0 1/2  Muon neutrino	<math><0.00000012</math> 0 1/2  Tau neutrino	80,379 +/-1 1  W boson	* All masses are given in MeV/c ²		

Figure 1.1: Periodic table of particles and intermediate particles of interactions of SM[1].

1.1.1 Quarks, leptons, and hadrons

Strongly interacting particles are composed of elementary particles with spin $\frac{1}{2}$ called *quarks*. Quarks arise in pairs together with antiquarks and at sufficiently large distances the mechanism known as color confinement occurs, when the energy in the bond of the quark-antiquark pair is so great that the bond can break and a new quark-antiquark pair is formed. Due to the color confinement, the range of the strong interaction is of the order of 1 fm. Quarks can bind together into hadrons in two ways – baryons and mesons. Quarks are found in 6 types, which are distinguished by the flavor of the quark and are arranged in pairs into three generations.

$$\begin{pmatrix} e \\ d \end{pmatrix}$$

$$\begin{pmatrix} c \\ s \end{pmatrix}$$

$$\begin{pmatrix} b \\ t \end{pmatrix}$$

Leptons are fermions, i.e. particles with spin $\frac{1}{2}$, which follow the Pauli exclusion principle. Leptons are created by pair production, this is expressed by the fact that lepton numbers are conserved.[14] They are subject to electromagnetic, weak, and gravitational interactions, but do not carry a color charge and therefore do not interact strongly. We distinguish 3 generations of leptons together with their corresponding antiparticles.

$$\begin{pmatrix} e \\ \nu_e \end{pmatrix} \qquad \begin{pmatrix} \mu \\ \nu_\mu \end{pmatrix} \qquad \begin{pmatrix} \tau \\ \nu_\tau \end{pmatrix}$$

Hadrons are particles composed of quarks and antiquarks that interact strongly. Hadrons are further divided into baryons composed of three quarks (fermions) and mesons composed of a quark-antiquark pair (bosons). An important group of hadrons is strange particles that decay through the weak interaction and charm hadrons that contain a c quark in pair with a total charm of 0 ($c\bar{c}$) or a total charm different from 0. The charm of c quarks was first observed in 1974 in experiments at the SLAC and BNL accelerators, in which a resonance with a mass of 3097 MeV was discovered. The team led by Burton Richter at SLAC named this particle ψ , while Samuel C. Ting's team at BNL named it J . The particle composed of the pair $c\bar{c}$ is currently known as J/ψ . [14]

The *Higgs boson* is also worth mentioning. It is a scalar particle with no electric charge, does not carry a color charge, and has spin 0. The Higgs boson is an expression of the Higgs field that generates the mass of all elementary particles. The mass of the Higgs boson is $m_H = 125.25 \pm 0.17$ GeV.[16]

1.1.2 Interactions

We distinguish 4 fundamental types of interaction: weak, strong, gravitational, and electromagnetic, all known interactions are governed by some combination of these four fundamental forces. Interactions are characterized by their range, potential, strength of interaction, and type of intermediate particles. SM describes 3 of these fundamental interactions, gravitational interaction is not included. The description of electromagnetic field, which can be described as the emission of photons, where the field propagated by the electric charge is associated with the existence of the charge and exists by itself in the form of an electromagnetic wave (this wave can be described as a photon flux, see Section 1.3 below), led to the generalization of the exchange character for other types of interactions.

Thus, the intermediate particle for the electromagnetic interaction is the photon, the immaterial boson with spin 1. The range of the interaction is infinite and affects the particles with non-zero electric charge or non-zero magnetic moment (neutron). The electromagnetic interaction is described by quantum electrodynamics (QED). The binding constant $\alpha_{em} = \frac{1}{137}$ does not change.

For gravitational interaction, so far unobserved graviton should be the intermediate particle. Graviton should be immaterial with no electric charge. The range of the interaction is also infinite and affects all known particles.

Three bosons W^\pm and Z^0 are intermediate particles for the weak interaction. The range of the interaction given by the mass of intermediate bosons is of the order of 10^{-3} fm. Interaction affects all quarks and leptons at small distances. The strength of the interaction is $\approx 10^{10}$ times smaller than that of the strong interaction. The weak interaction is the only interaction that allows processes in which the quark flavor changes and some other quantum numbers (strangeness, charm, or parity) do not have to be preserved. According to [16] the masses of intermediate bosons are: $m_{W^\pm} = 80.377 \pm 0.012$ GeV and $m_{Z^0} = 91.1876 \pm 0.0021$ GeV.

Intermediate particles for strong interaction are 8 gluons. A gluon is an immaterial boson with no electric charge and carries a color charge, a property of quarks and gluons. We distinguish between three color charges - R, G, and B, and their corresponding anticolors. A color-neutral combination is created by combining the appropriate color and anti-color.

The strong interaction, that binds quarks and also protons and neutrons within a nucleon, affects only particles with a colored charge and is described by the physical theory of Quantum Chromodynamics (QCD). The quantum numbers of strangeness, charm, beauty, truth, and baryon number are conserved in strong interactions. As mentioned before the range of the strong interaction is due to color confinement of the order of 1 fm. Considering the fact that the coupling constant decreases with decreasing distance, then quarks close to each other can move almost freely, this is referred to as asymptotic freedom and is also the reason to study the properties of quark-gluon plasma during the collisions of two nuclei. The description is often performed by the perturbation theory of quantum chromodynamics, where the interaction terms of the Lagrangian are expanded in power series in powers of the coupling constant due to the complexity of the Lagrangian. If this constant is small, we can limit ourselves to the first few terms, most often the first term (leading order), and consider the others as a small perturbation of the first term. This expansion can only be used for small values of $\alpha_S \ll 1$ and thus for large values of Q, where Q is transferred four-momentum.

Coupling constant as a function of Q^2 is given by

$$\alpha(Q^2) = \frac{\alpha(\mu^2)}{1 - \frac{\alpha(\mu^2)}{3\pi} \ln \frac{Q^2}{\mu^2}}, \quad (1.1)$$

where μ^2 is the initial scale when we know the value of the coupling constant. The scale can be determined from the condition $\alpha(0) = \frac{1}{137}$.

1.2 Ultra-peripheral collisions

In high-energy nuclear physics, we can study the properties of nuclear matter in the order of high energies with the main interest in heavy-ion collisions. Collision that occurs at an impact parameter, larger than the sum of nuclear radii of the interacting particles in the presence of a strong electromagnetic field is denoted as an Ultra-Peripheral Collision (UPC), where the impact parameter is the perpendicular distance from the center of the target nucleon to the line of flight of the incident nucleon field. This type of collision therefore takes place outside the range of strong interaction and hadronic interactions are strongly suppressed. Thus this type of collision is governed by electromagnetic forces. Like gravity, the electromagnetic interaction between two objects acts at an infinite distance and decreases with the square of the distance. Heavy ions are a source of coherent electromagnetic fields (coherence of electromagnetic field indicates the similarity of the field at two different points in space and time) and due to the infinite range of electromagnetic interaction, the interaction can occur at relatively large separation distances of ions.[17] Illustration of UPC of two highly charged, fast-moving ions of charge Z_1 , Z_2 , and radii R_1 , R_2 at impact parameter $b > R_1 + R_2$ with the electric field vector pointing in a direction perpendicular to the motion of the ions (radially outwards) with magnetic field surrounding the ion trajectory is shown in Figure 1.2. At high speeds, electric and magnetic fields are nearly perpendicular. Information for this chapter is drawn from [2].

UPC of two ions provides opportunities for studying electromagnetic processes. Hadron colliders like Relativistic Heavy Ion Collider (RHIC) produce photonuclear and two-photon interactions at high luminosities and energies and allow to study of photon-nucleus and photon-photon collisions. In photon-hadron interactions, the production of J/ψ meson can occur the same as the production of other mesons (Υ , ρ^0 , ϕ , and ω) or jets.[2]

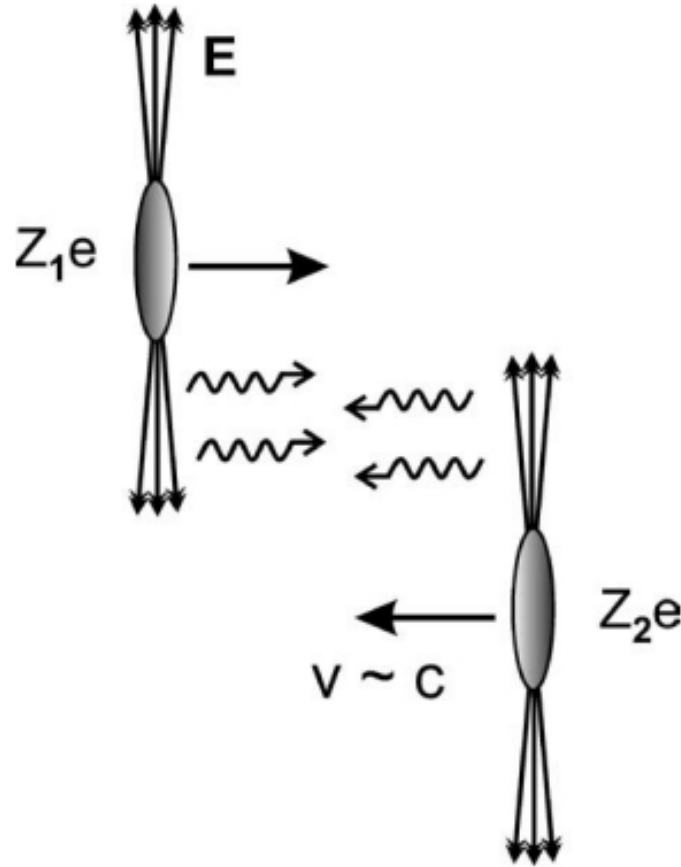


Figure 1.2: UPC of two highly charged, fast-moving ions Z_1 , Z_2 [2].

1.3 Photon flux

Electromagnetic fields of charged, fast-moving particles can be treated as a flux of virtual photons, this method of treatment is known as the equivalent photon method. Virtual (nearly real) photons do not exist indefinitely, they have finite effective mass m and a lifetime $\tau = \hbar/mc^2$. If their mass is low and their lifetime is long enough, we can treat photons as real.[3] The number of photons $n(\omega)$ with energy ω is given by the Fourier transform of the time-dependent electromagnetic field.[2]

Reactions are then mediated by the Exchange of virtual photons with a number of photons scaling with nuclear charge squared and photon energies scaling with the Lorentz contraction of the nuclei and increasing with beam energy.[18]

In the collision of two nuclei, two situations can occur. In the first case, a photon from one ion can interact with a second ion or two photons, each from one ion will interact with the other in a photon-photon interaction. Due to the very strong electromagnetic field, multiple photon excitation of nuclear target is possible and high photon energies can be used to study the gluon density in heavy nuclei. These two situations are shown in Figure 1.3.

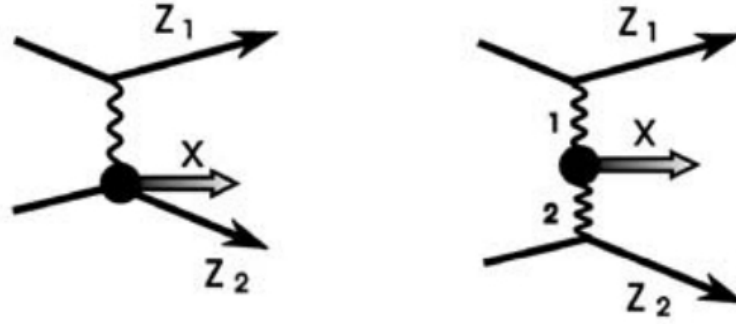


Figure 1.3: One photon (left) and two-photon interaction (right) in heavy ion collision[2].

The photoproduction cross section σ_X of a final state X is given by

$$\sigma_X = \int d\omega \frac{n(\omega)}{\omega} \sigma_X^\gamma(\omega), \quad (1.2)$$

where $\sigma_X^\gamma(\omega)$ is the photon-nucleus photoproduction cross and $n(\omega)$ is number of photons with energy ω .

Unlike fixed target accelerators, photon-heavy ion collisions will reach 30 times more energies.[2]

The cross section for photon-photon processes is given by

$$\sigma_X = \int d\omega_1 d\omega_2 \frac{n(\omega_1)}{\omega_1} \frac{n(\omega_2)}{\omega_2} \sigma_X^{\gamma\gamma}(\omega_1, \omega_2), \quad (1.3)$$

where $\sigma_X^{\gamma\gamma}(\omega_1, \omega_2)$ is the two-photon cross section.

Two-photon process can be usable for meson spectroscopy, testing of QED, or at the highest energy colliders to investigate the content of quarks and spin structure of meson resonances. If there is a situation of excitation of the nucleus through Coulomb excitation in a multi-photon process, then we cannot consider the emission of each photon as independent. In multiple photonuclear interactions, the polarization of the photons emitted by the nuclei also plays a role. All photons from the same nucleus will have the same polarization in the direction of the nucleus field vector, which corresponds to the direction of the impact parameter vector. The polarization of photons emitted by the second nucleus will be opposite.[2] Important aspects of two-photon flux are, that radial position magnitudes are both greater than radii.[19]

Due to the Lorentz contraction, the nuclei moving towards each other have oblate deformation together with their fields, the electric field is linearly polarized with a magnetic field circulating around. Electric and magnetic fields determine the energy spectrum of the photon flux. Increasing the density of the electric field leads to photons with higher energy.[19]

In the lab frame, the maximum photon energy is

$$\omega^{max} = \frac{\hbar}{\Delta t} \sim \frac{\gamma \hbar v}{b} \quad \gamma = \frac{1}{\sqrt{1 - \frac{v^2}{c^2}}}, \quad (1.4)$$

where γ is the Lorentz factor, Δt is the interaction time, v is the projectile velocity and b is the impact parameter.

The type of particles produced in interaction also depends on the orientation of the electric field of each ion. If the orientation of electric fields is parallel, the result will be scalar particles, i.e., particles with spin 0 and even parity. For perpendicular orientation, we will get particles with spin 0 and odd parity, therefore pseudo-scalar particles.

Events from UPC are usually fully reconstructed and because of the small transverse momentum of photon ($p_T \approx \omega/\gamma c$), the transverse momentum of the final state will be also small. The production of the vector meson occurs in photonuclear interaction that involves coherent scattering. Also in this process, the transverse momentum of the final state will be small.

RCE (Relativistic Coulomb Excitation) in which the projectile and the target nuclei can exchange one or more photons can be used to investigate the dynamics and structure of colliding nuclei. In heavy-ion colliders, Coulomb excitation of the ions leads to simultaneous fragmentation of the ions and can be used for beam monitoring.[2]

1.4 Exclusive Particle Production

We talk about exclusive particle production when the nucleons or nuclei in the interaction remain in their ground state or are only internally excited. Exclusive particle production is a coherent interaction of a photon from the projectile with the field of the target resulting in the production of vector meson and nothing else. The result of this primarily coherent interaction is most likely the production of a vector meson because the photon has negative parity and spin 1.[18] Therefore UPC can be classified into one-photon and two-photon processes. One photon processes include coherent diffractive production of exclusive vector mesons.[19] Two-photon processes include exclusive dilepton production (electrons and muons). The cross-section of vector meson production in A+A interaction can be calculated from Equation 1.2. By changing photon energy ω to rapidity y and using the relation $\omega = \frac{M_V c^2}{2} e^y$ we obtain[2]

$$\frac{d\sigma(A + A \rightarrow A + A + V)}{dy} = n(\omega) \sigma_{\gamma A \rightarrow V A}(\omega), \quad (1.5)$$

where M_V is the mass of the vector meson.

According to the Generalized Vector Meson Dominance Model (GVMD)[20], the scattering amplitude for the process $\gamma + A \rightarrow B$ is the sum of the corresponding

vector meson scattering amplitudes. For elastic scattering $\gamma + A \rightarrow V + A$, the cross-terms are usually small and are often neglected.[2] The cross section is then

$$\frac{d\sigma(\gamma + A \rightarrow V + A)}{dt} = C_V^2 \frac{d\sigma(V + A \rightarrow V + A)}{dt} \quad C_V = \frac{\sqrt{4\pi\alpha_{em}}}{f_V}, \quad (1.6)$$

where $d\sigma/dt = |A|^2$, t is the momentum transfer from the target nucleus squared and C_V are coefficients related to the photon-vector meson coupling f_V with numerical values determined from decay widths from vector meson leptonic decay.

From two-gluon exchange in QCD was calculated the forward scattering amplitude for heavy vector mesons in the interaction of a photon with a single nucleon as

$$\left[\frac{d\sigma(\gamma p \rightarrow V p)}{dt} \right] \Big|_{t=0} = \frac{\alpha_s^2 \hbar^2 \Gamma_{ee}}{3\alpha_{em} M_V^5 c^6} 16\pi^3 [xg(x, M_V^2/4)]^2, \quad (1.7)$$

where x is the fraction of the proton or nucleon momentum carried by the gluons, α_s is the strong coupling constant, α_{em} is the electromagnetic coupling constant, Γ_{ee} is decay width from di-electronic decay and $g(x, Q^2)$ is the gluon distribution evaluated at $Q^2 = M_V^2/4$.

The cross section 1.7 from the two-gluon exchange is usable due to the fact that photon can fluctuate into quark-antiquark pair and interact with the nucleus (see Section 1.6). This simplification with only one nucleon interacting with a photon can be used to determine cross section for interaction of a photon with the whole nucleus. Also, the photoproduction cross section rises fast with increasing energy. Figure 1.4 shows the prediction of $d\sigma/dt$ for J/ψ in Au+Au collision.

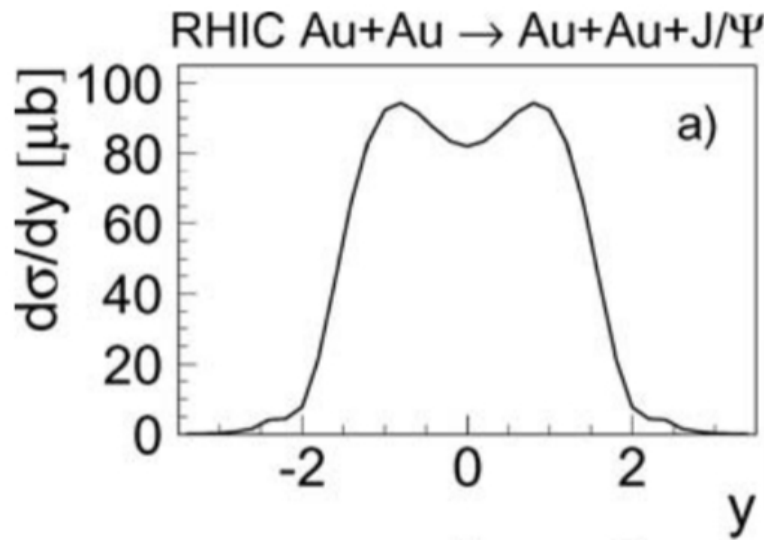


Figure 1.4: Prediction of $d\sigma/dt$ for J/ψ in Au-Au collision at RHIC[2].

1.4.1 Interference in Exclusive Vector meson Production

Due to the fact that we are not able to distinguish between a projectile and a target nucleus, and in the case of swapping the situations are indistinguishable. In these two situations when one nucleus emits a photon and through interaction with a second nucleus vector meson is produced or a second nucleus can emit a photon and the same vector meson can be produced we cannot simply add cross section for both possibilities leading to the same final state. The cross section by adding the corresponding amplitudes depending on photon flux and rapidity A_1 and A_2 is

$$\frac{\hbar d\sigma}{dy dp_T} = \int_{b>2R} |A_1 \pm A_2|^2 d^2b, \quad (1.8)$$

where A_1 and A_2 are corresponding amplitudes determined by the longitudinal momentum of the final state vector meson[3].

Interference is maximal at mid-rapidity, where $A_1 = A_2$ and for ion-ion collisions because vector meson has negative parity interference is destructive. If we treat the outgoing vector meson as a plane wave the interference at mid-rapidity is

$$|A_1 \pm A_2|^2 = 2A_0^2 \left(1 \pm \cos \left(\frac{p \cdot b}{\hbar} \right) \right). \quad (1.9)$$

In ion-ion collisions at low momentum p_T , as $p_T \rightarrow 0$ interference disappears but is significant for $p_T < 250$ MeV/c for the J/ψ . [2]

Interference is of interest because of the very short lifetime of vector meson compared with impact parameters. Vector meson cannot be produced outside of the range of strong interaction, which is ≈ 1 fm, because it is a result of quark-antiquark pair interaction with the nucleus (Section 1.6). An example of interference in a number of ρ^0 mesons production is shown in Figure 1.5

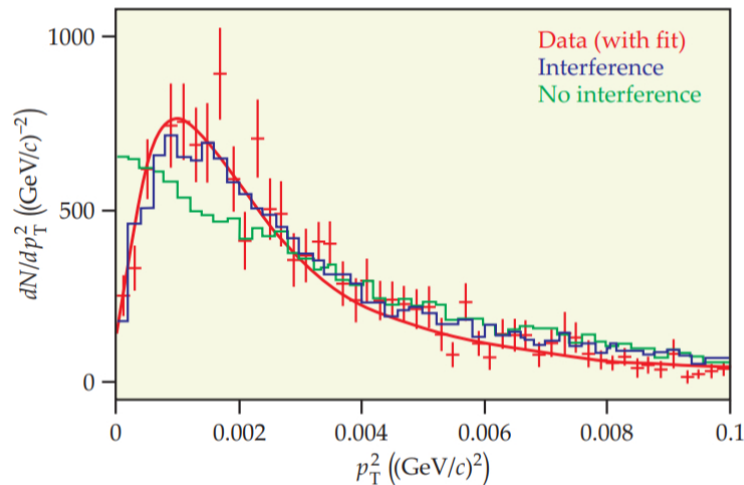


Figure 1.5: The STAR collaboration observed interference in the production of mesons ρ^0 at transverse momentum p_T [3].

1.4.2 Non-UPC

Non-UPC events are events with the final state associated with UPC.

Exclusive events mean that there is no other activity observed by a detector with large acceptance, however, nuclei are easily excited allowing for event tags using forward neutrons. In most exclusive events, the nuclei emerge intact and no neutrons are emitted. ZDC therefore cannot decide the primary process (if dilepton production was photonuclear or $\gamma + \gamma$ interaction in origin).[19]

1.5 Inclusive Photoproduction

Unlike exclusive particle photoproduction, if at least one of the nucleons or nuclei breaks up. the particle production is inclusive. The high rate of photonuclear interactions at hadron colliders is the result of the high photon flux and total photon-hadron cross section. At RHIC in Au+Au collisions, the total photonuclear cross section for the photon-nucleon center of mass energies above 4 GeV is about 2 barns.[2]

We are interested mainly in the production of heavy quark-antiquark pairs as it will contribute to signal for J/ψ . As the photon interacts with the target nuclei with parton and the partonic cross section calculated from QCD will be

$$\sigma_{\gamma g \rightarrow q\bar{q}}(W_{\gamma g}) = \frac{\pi e_q^2 \alpha_{em} \alpha_s(Q^2) \hbar^2 c^2}{W_{\gamma g}^2} \left[(3 - \beta^4) \ln \left(\frac{1 + \beta}{1 - \beta} \right) - 2\beta(2 - \beta^2) \right], \quad (1.10)$$

where $\beta = (1 - 4m_q^2 c^4 / W_{\gamma g}^2)^{1/2}$, m_q and e_q are mass and electric charge of quark and $W_{\gamma g}$ is the photon-gluon center-of-mass energy. If the gluon carries a fraction x of the nucleon momentum, then $W_{\gamma g}^2 = 2\omega x \sqrt{s}$. The strong coupling constant $\alpha_s(Q^2)$ is evaluated at $Q^2 = m_q^2 c^2 + p_T^2$, where p_T is the quark transverse momentum.

Given by convolution of Equation 1.10 with the photon flux $n(\omega)$ and the nucleon gluon distribution, the total photoproduction cross section is

$$\sigma [A [\gamma] A \rightarrow Aq\bar{q}X] = \int \int \frac{n(\omega)}{\omega} G^A(x, Q^2) \sigma_{\gamma g}(W_{\gamma g}) \Theta(W_{\gamma g} - 2m_q c^2) d\omega dx, \quad (1.11)$$

where $G^A(x, Q^2)$ is gluon distribution.

Equation 1.11 is equivalent to Equation 1.3 for two-photon interactions, where photon flux is replaced with gluon distribution. At RHIC mid-rapidity production of $c\bar{c}$ pair in heavy-ion collisions probes x -values $x \sim 2 \cdot 10^{-2}$. The value of gluon x and the photon energy have an influence on the rapidity of heavy quark-antiquark production. In the production of $c\bar{c}$ pair, also shadowing will have a considerable influence on the production.[2]

1.6 Photoproduction

Photoproduction at hadron colliders can serve as a tool for examining gluon distribution due to the fact that photons couple weakly to charged particles and not to themselves. They are therefore usable to study the internal structure of proton and heavier nuclei.[3] In particular in interaction when heavy vector meson is produced, photoproduction of heavy quark-antiquark pairs and photoproduction of jets. Gluon density can be written as

$$G^A(x, Q^2) = Ag(x, Q^2), \quad (1.12)$$

where $g(x, Q^2)$ is the nucleon gluon distribution, x is the fraction of momentum carried by the gluon, Q^2 square of the 4-momentum transfer and A is the number of nucleons.

Distribution increases rapidly as x decreases.

However, deviation from Equation 1.12 has been observed. Depending on the value of x , suppressions (shadowing) of up to $\sim 30\%$ and enhancements (ant-shadowing) of up to $\sim 10\%$. Better measurement of $G^A(x, Q^2)$ can be obtained from photoproduction at heavy-ion colliders.[2]

In UPCs, the photoproduction of vector mesons can be described by

- Photon fluctuation to a virtual quark-antiquark pair,
- Interaction of pair on the nuclear target,

with the scale of photoproduction given by masses of mesons.[4]

In photonuclear interaction, vector meson is reconstructed from decay products and in a two-photon process decaying to a di-lepton pair. Events are characterized by very low transverse momentum.[18]

Interaction, when a photon interacts with the whole nucleus, is called Coherent photoproduction. Coherent photoproduction resulting in dilepton or vector meson corresponds to $p_T = 60$ MeV/c. Also, additional interactions between the nuclei because of intense electromagnetic fields can lead to the excitation of one or both nuclei, resulting in the emission of at least one neutron in the direction of emitting nucleus.[18]

Inelastic hadronic interactions involve fluctuation of the photon into a quark-antiquark pair, particle production is in the direction opposite to the photon. Interaction can be both direct, when a photon interacts directly with a gluon in the target nucleus, or resolved with the photon fluctuating to a parton shower and one of the shower products interacting with either a quark or gluon in the target.[19]

1.6.1 Proton's gluon distribution

As mentioned above, a photon can interact with a charged particle through electromagnetic interaction, or it can fluctuate into a virtual hadronic state and interact with the nucleus through strong interaction. The quark-antiquark pair subsequently scatters on the target nucleus and a real vector meson emerges, i.e. the bound state of the quark-antiquark pair. Hadronic states are the main contributor to the total photonuclear cross section. The situation of the interaction of a virtual meson with a target nucleus for a low-energy photon can be viewed as an exchange of another meson - a pomeron. A pomeron is composed of gluons (possibly quarks), is colorless, interacts through strong interaction, and has quantum numbers of vacuum.[17] In the simplest model, the exchange of a pomeron corresponds to the exchange of two gluons.[3]

The cross section in the two-gluon scattering is proportional to the square of the gluon distribution

$$\sigma \propto [x \cdot g(x, Q^2)]^2 \quad (1.13)$$

Vector meson photoproduction is therefore sensitive to gluon content in nuclei. At low Bjorken- x gluon distribution can be described by a power law $x \cdot g \propto x^{-\lambda}$, $x = (M_V c^2 / W_{\gamma p})$, where $W_{\gamma p}$ is the photon-proton center of mass energy and $M_V c^2$ is mass of the vector meson. Combining Equation 3.1 with power law we get

$$\sigma \propto W_{\gamma p}^{4\lambda} \quad (1.14)$$

The cross section for the reaction $\gamma + p \rightarrow J/\psi + p$ does follow a power law and the value of α is determined from measurements as $4\lambda = 0.7$ for values of x in range from $2 \cdot 10^{-5}$ to 10^{-2} . [3]

In this observation, we considered only the interaction of a photon with a single nucleon (proton) instead of a heavy ion composed of several nucleons in the production of a vector meson. The cross section determined from the interaction with only one photon can be used to determine the gluon distribution function and the cross section of the photon interaction with the whole nucleus, when quark-antiquark pair can interact more than once while going through the target, resulting in vector meson production. Cross section for this process scales approximately as A^2 . [3]

1.6.2 Photoproduction of J/ψ

Due to the higher mass of J/ψ , which is 3096.900 ± 0.006 MeV[16], photoproduction occurs on a harder scale. During the process, the photon fluctuates into the dipole of the $c\bar{c}$ pair and interacts with the target nucleus. The effect of shadowing can deplete the nuclear gluon density, this effect can be investigated on coherent photoproduction of J/ψ at low values of Bjorken- x , where $x = \frac{p_{parton}}{p_{hadron}}$. STAR probes the gluon distribution at $x \approx 0.015$. Selection criteria for $J/\psi \rightarrow e^+e^-/\mu^+\mu^-$ are the very central rapidity region $|y| < 0.02$ to prevent cosmic background, just two tracks from the decay. Background from two-photon production of dilepton pair is also present[4]. In Figure 1.6 is shown cross section of J/ψ as a function of transverse momentum.

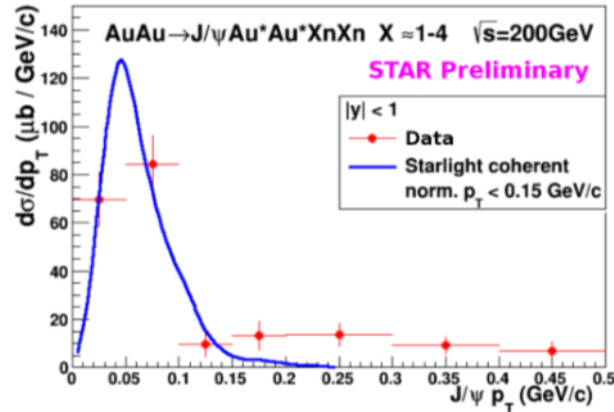


Figure 1.6: J/ψ cross section as a function of transverse momentum p_T [4].

Selection criteria for e^+e^- are to get a two-track event in an otherwise empty detector (except very forward neutrons). From 13000 of e^+e^- , only ~ 10 candidates are present in the data for $J/\psi \rightarrow e^+e^-$ [4].

Exclusive J/ψ production showed that the density of gluons carrying a small fraction of the momentum of hadrons grows extremely rapidly and is slowed down by gluon saturation.[18]

Photon coupling can be coherent or incoherent and therefore the signal of J/ψ consists of a coherent and incoherent signal for J/ψ , and also of the contribution from dielectron pair production, which can be a result of two-photon interaction and not the decay of J/ψ . Coherent and incoherent signals of J/ψ have different shapes of the p_T spectrum.

1.7 Two-photon production

The interaction of fast photons can lead to the pair production of dileptons. Namely, e^+e^- , $\mu^+\mu^-$ or $\tau^+\tau^-$ with dominant production of e^+e^- pair than production of heavier pairs like $\mu^+\mu^-$ and $\tau^+\tau^-$. Production of a bound free particle is also possible (for example only e^+), this particle is then captured by one nucleus leading to possible limitation of luminosity in the collider.[19]

STAR studied the two-photon production of di-lepton pair and their invariant mass in the range from 0.1 GeV to 100 GeV. The experimental measurements are in excellent agreement with lowest-order QED calculations and thus set important limits on the contributions from higher-order processes. The cross section for electron-positron pair production is about 30 000 times higher for photon-photon encounters than for hadronic interactions. Dilepton production in two-photon interactions may be used to measure the beam luminosity or to extract the efficiency of the particular trigger aimed for exclusive events with dilepton decay of the J/ψ . [3]

In the case of inclusive photoproduction two-photon interactions will also contribute to $q\bar{q}$ pair production process but with a smaller contribution compared to the direct production cross section. The cross section for $q\bar{q}$ pair production is given

by Equation 1.3[2].

1.7.1 Free e^+e^- pairs production

The process of e^+e^- pairs production can involve multiple photon exchange (Coulomb distortion) and the production of several e^+e^- pairs. Heavy ions can go through several electromagnetic reactions in one interaction because of the large charge of colliding ions. If the energy loss by the nucleus is not significant we can treat each photon emission independently. For heavy ions, the probability of e^+e^- is close to one. Cross section of e^+e^- production in relativistic collisions of fast particles is given by[2]

$$\sigma = \frac{28}{27\pi} \sigma_0 [L^3 - 2.198L^2 + 3.821L - 1.632], \quad (1.15)$$

where $\sigma_0 = (Z_1 Z_2 \alpha^2 \hbar / m_e c)^2$, $L = \ln(\gamma_1 \gamma_2)$ and $\gamma_{1,2}$ is The Lorentz factor of ion 1,2 in the laboratory system.

To this equation, we need to add a correction term for Coulomb distortions which is

$$\sigma_C = -\frac{28}{9\pi} [f(Z_1 \alpha) + f(Z_2 \alpha)] \sigma_0 L^2, \quad (1.16)$$

where

$$f(x) = x^2 \sum_{n=1}^{\infty} \frac{1}{n(n^2 + x^2)} \quad (1.17)$$

is the Bethe-Maximon correction.

1.7.2 Meson Production in Two-Photon interactions

In two-photon production of meson, there is a requirement of relatively large energy (for lightest mesons π^0 energy ≥ 70 MeV) and small impact parameters (compared to $2R_A$) for mesons to be produced. We can rewrite the equation for cross section 1.3 and get

$$\sigma_X = \int ds \frac{d\mathcal{L}(W_{\gamma\gamma})}{dW_{\gamma\gamma}} \sigma_{\gamma\gamma \rightarrow X}(W_{\gamma\gamma}), \quad (1.18)$$

where $W_{\gamma\gamma} = 4\omega_1\omega_2$ is the square of the center-of-mass energy of the two photons, $\sigma_{\gamma\gamma \rightarrow X}(W_{\gamma\gamma})$ is the two-photon production of particle X, and $d\mathcal{L}(W_{\gamma\gamma})/dW_{\gamma\gamma}$ is the photon-photon luminosity, which can be multiplied by the ion beam luminosities to obtain two-photon luminosity.

Due to the different strengths of coupling constant for strong and electromagnetic interactions, the cross section in two-photon production of mesons is different than values for photonuclear vector meson production. It can be also problematic to recognize certain events because of the large background from photonuclear interactions. For example, the photoproduction rate of J/ψ , which is followed by $J/\psi \rightarrow \gamma \eta_c$ can be longer than the rate of $\gamma\gamma \rightarrow \eta_c$. [2]

Chapter 2

Experiment STAR at RHIC

The content of the following chapter is devoted to Brookhaven National Laboratory and its complex with the relativistic heavy ion collider used for heavy ion collisions. Subsequently, emphasis is placed on one of the experiments on the collider, the STAR experiment, from which the data processed in the following chapter originates.

2.1 BNL

Brookhaven National Laboratory (BNL) is a Department of Energy national laboratory established in 1947 at Camp Upton on Long Island in New York state. It used to be one of the United States military bases and after World War II the military base was closed and a laboratory was established. The main motivation for the establishment of the laboratory was peacetime research on atomic energy and the construction of a nuclear reaction near New York City. In 1946 several nonprofit corporations and universities were established that participated in the establishment of the laboratory. Information for this section is based on [21] and [22].

At BNL there is ongoing research including nuclear and high-energy physics, bioscience, and nanoscience, which take place in the BNL area, consisting of several facilities. Some of the facilities are listed below and shown in Figure 2.1.

- Relativistic Heavy Ion Collider (RHIC) is the first machine in the world capable of colliding heavy ions and the only collider capable of colliding beams of polarized protons of high energies. Head-on ions of gold traveling at almost the speed of light are primarily used in collider which was designed to research quark-gluon plasma. RHIC is discussed more in the following subsection.[23]
- The Electron Ion Collider is a newly planned project at BNL that will be using parts of RHIC with two interaction regions with detectors. The aim of the accelerator is to investigate the properties of nuclei and their connection with the quarks and gluons of which they are composed.[23]
- The NASA Space Radiation Laboratory (NSRL) operating since July 2003 as part of the NASA space program. NSRL can accept a range of ions from BNL's

Booster accelerator with energies from 0.05 to 3 GeV/nucleon and simulates the biological effects of the cosmic rays found in space using beams of ions.[24]

- National Synchrotron Light Source II (NSLS-II) which replaced the previous Synchrotron Light source (NSLS) is BNL's newest facility operating since 2015. NSLS-II enables the study of material properties and research of synthesis and production of materials and environment.[25]

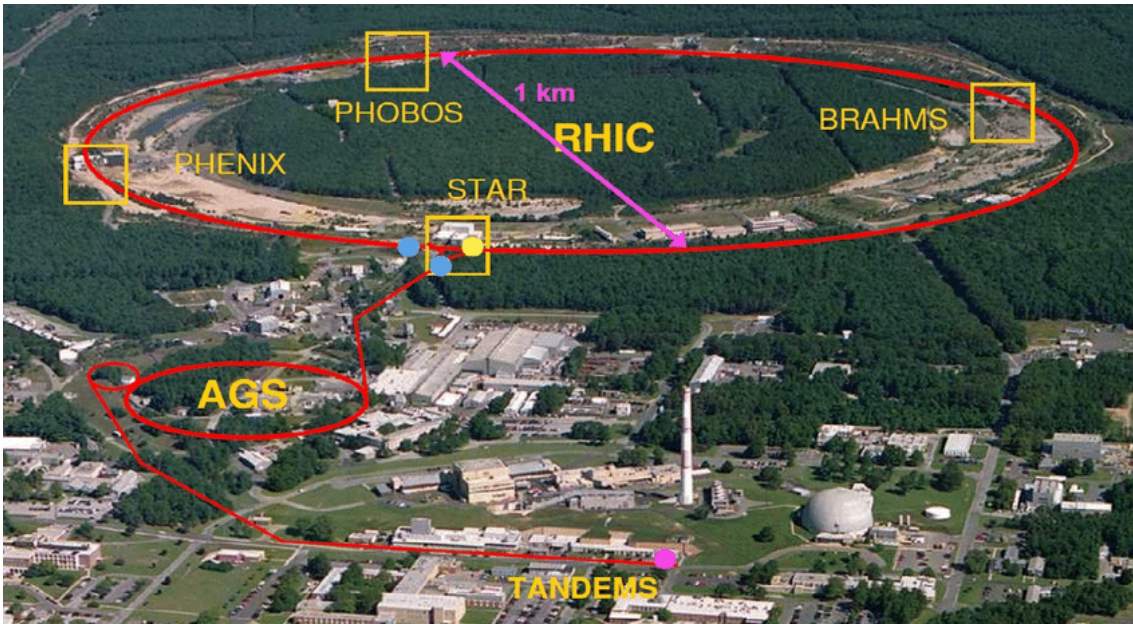


Figure 2.1: BNL heavy-ion collider complex overview [5].

2.2 RHIC

Relativistic Heavy Ion Collider (RHIC) as was stated before is the collider capable of colliding heavy ions and the only collider in the world capable of colliding beams of spin-polarized protons. RHIC became operational in 2000 as a successor to the canceled ISABELLE accelerator project. ISABELLE – proton beam accelerator with energies of 200 x 200 GeV, later increased to 400 x 400 GeV with a ring circumference of 3.8 kilometers and superconducting magnets with a strength of 5 T. The ISABELLE project ran into technical difficulties with the magnets. This later led to the conversion of ISABELLE to the construction of a heavy ion accelerator. Information for this section is based on[21] and [6].

The accelerator system also includes 4 sets of detectors, namely BRAHMS, STAR, PHOBOS, and sPHENIX, the successor to PHENIX with only STAR and sPHENIX currently operating. The accelerator enables head-on proton-proton collisions at almost the speed of light at the energy of 250 GeV, as well as ion-ion collisions with energies reaching 100 GeV per nucleon per beam and with the maximum center of mass energy for Au+Au collisions $\sqrt{s_{NN}} = 200$ GeV per nucleon.

[26] In ion-ion collisions mainly gold ions are used, but other lighter ions such as aluminum, helium, copper, zirconium, ruthenium, or uranium.

The accelerator itself consists of two independent quasi-circular rings of superconducting magnets with a circumference of 3,8 km "Blue and Yellow Ring", the Blue ring for the beams oriented clockwise and the Yellow beam for the counterclockwise direction. Rings serve to accelerate or store particles. Collisions in the accelerator occur at six interaction points, in the center of the arc sections and insertion section for each ring. A pair of dipole magnets DX and D0 are used to direct the beams for a head-on collision. Furthermore, three quadrupole magnets Q1, Q2, and Q3 are used to focus the beam.

Acceleration starts at the ion source and Tandem strippers. At the Tandem Van de Graaff, the atoms are partially stripped of electrons with a stripping foil and the accelerated ions with energy of 1 MeV per nucleon[27] continue to the Booster Synchrotron, where they are accelerated to an energy of 95 MeV per nucleon.[26] After further stripping, the ions are split into 24 bunches and injected into the AGS for acceleration to be injected into the RHIC with an injection energy of 10 GeV per nucleon. Before injections are ion also debunched and then re-bunched before injection to RHIC leaving AGS. RHIC uses Radio Frequency (RF) systems to capture bunches from AGS and for acceleration.

For the case of polarized protons, a different approach is needed due to the problematic maintenance of polarization with increasing energy. Protons are injected from a 200 MeV Linac and Siberian Snakes are used to maintain beam polarization. The overall layout of the BNL accelerator complex and the layout of accelerator RHIC are shown in Figure 2.2 and Figure 2.3.

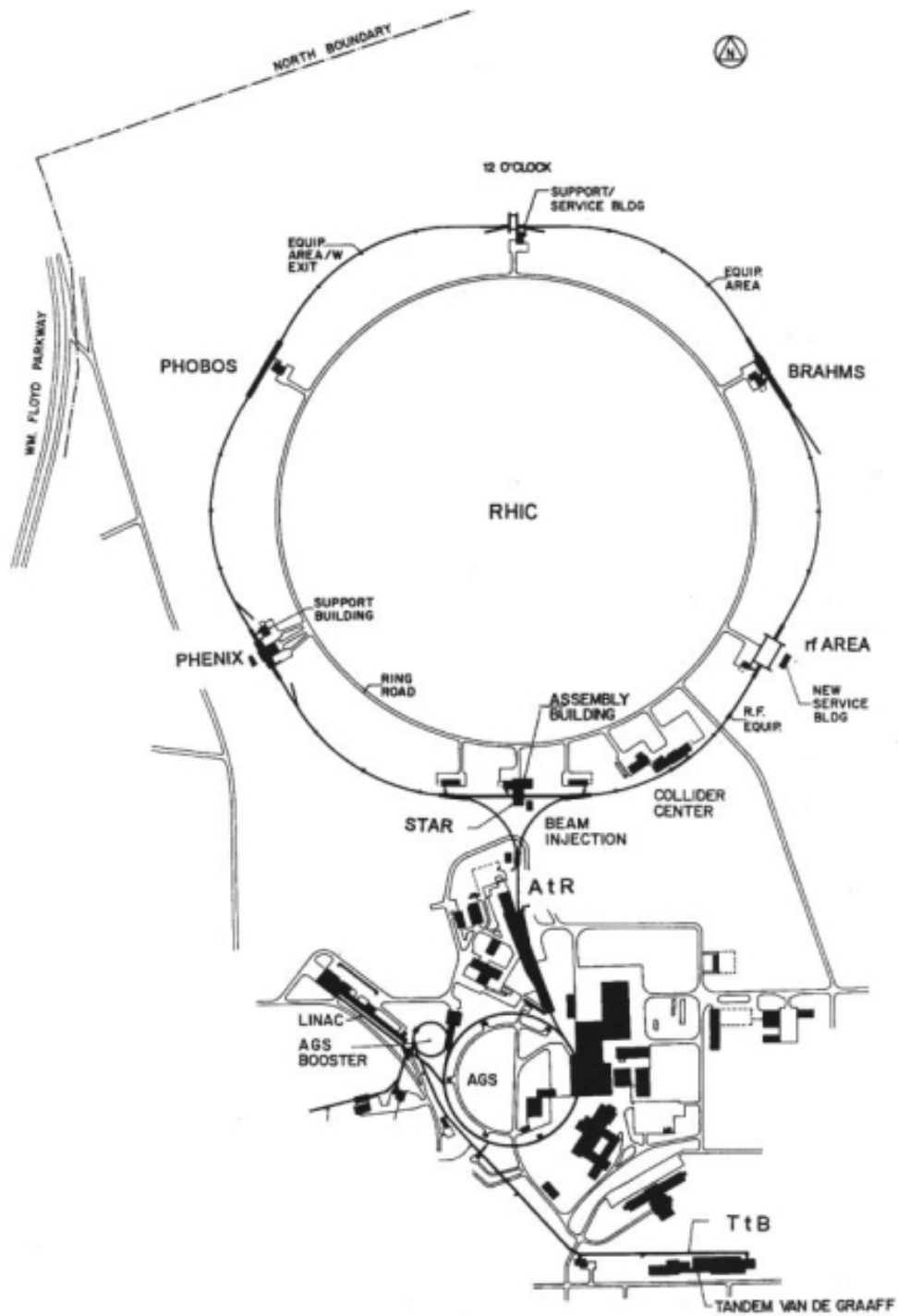


Figure 2.2: BNL accelerator complex layout[6].

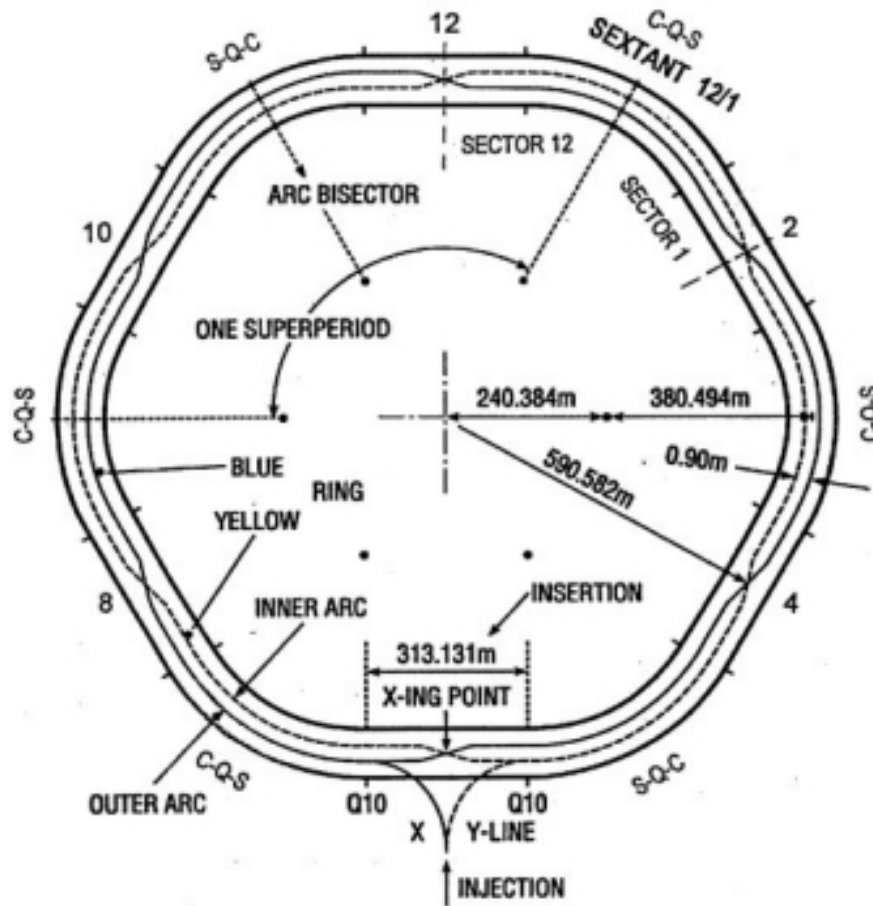


Figure 2.3: RHIC geometry layout [6].

2.2.1 Radio Frequency (RF) system

Information for this subsection is based on [28] and [29]. Acceleration using an rf cavity provides a longitudinal electric field with an rf frequency in the order of several hundreds of kHz with linacs producing long trains of beam pulses at rf. The electric field in the accelerator is therefore not static and oscillates in two opposite directions. The cavity is the volume or drift tubes in the accelerator into which radio waves are sent, which causes the electromagnetic field to oscillate. The resonant frequency depends on the shape of the cavity, and the energy in the form of a radio wave is amplified into an electromagnetic field. Rf cavities are structures where radio waves resonate. A particle beam consists of a series of very short groups of particles separated by a long distance, due to the fact that an electromagnetic field oscillates. A group of particles is called a bunch.

In heavy-ion booster linacs superconducting rf low-velocity accelerating cavities are being used designed to preserve the high beam quality, energy variability, and possibility to accelerate a wide variety of ions. Low operating frequencies are used

to make the structure as long as possible to maximize the accelerating voltage per structure. An accelerating electric field is associated with a changing magnetic field. Synchronization and phase focusing are needed to accelerate a bunch of charged particles. Synchronization is achieved by uniting the rf frequency with the particle velocity and phase focusing is achieved by choosing the phase angle between the rf wave and beam bunch. Modulation of the rf voltage is used to extract the beam with the required quality. To accelerate a particle, the rf frequency needs to be synchronized with the revolution frequency of the particle, i.e. it must be equal to the harmonic number h , determining the bunch spacing and the maximum number of particles per bunch, multiplied by the revolution frequency ω_0 , which is a function of the magnetic field and the radius of the accelerator.

Radio Frequency Quadrupole (RFQ) is also part of the rf system, which is a compact accelerator operating over a mass range of protons to low charge state heavy ions used as synchrotron and linac injector. In collider one can influence and change the parameters of an individual bunch or several bunches, this process is called rf gymnastics. Rf gymnastics is called adiabatic if the parameters of the synchrotron motion change slowly enough so that the particle distribution is in equilibrium during the process. Single bunch manipulation is a process during which the length and energy distribution of the bunch is changed.

We will now give a brief introduction to single or multiple-bunch manipulation in the collider.

Examples of single-bunch manipulations:

- Controlled longitudinal blow-up - a non-adiabatic process during which the beam is stabilized by reducing the longitudinal particle density while providing a well-defined distribution with sharp edges
- Bunch compression - an adiabatic decrease of bunch length and increase in energy spread resulting in a change of bunch parameters such as energy, voltage, etc., or a non-adiabatic method of bunch rotation, where the bunch is stretched and rotated around the center

Examples of multi-bunch manipulations:

- Debunching - the beam is initially divided into several bunches and is converted into a continuous beam without changing the density, this is an iso-adiabatic process by reducing the voltage
- Re-bunching - the number of bunches is divided by two with the aid of two rf systems, one with the initial frequency and the other with a frequency mostly half of the initial
- Coalescing - the unification of n bunches into a single one, the process is non-adiabatic and the initial and final states have the same rf frequency and harmonic number h

- Slip stacking - non-adiabatic process where two sets of bunches are united into one set, two rf systems with different frequencies are needed for the process
- Batch compression – process can be quasi-adiabatic, during the process, the space over which n bunches are distributed is changed, the number or shape of the bunches is preserved, more than two rf systems with a large frequency range is needed

2.2.2 Detectors at RHIC

As mentioned above, there are 4 detectors at RHIC, and only 2 currently operating. The location of individual experiments at RHIC can be seen in Figure 2.1.

- BRAHMS experiment at RHIC completed in 2001 and partly operated in 2000 was used to investigate the quark-gluon plasma during collisions of heavy ions with energies in the center of mass energies of 200 GeV per nucleon pair, covering the widest range in polar angle as possible. Designed with two moving magnetic spectrometers to measure charged particles in a large range of transverse momentum and rapidity. Spectrometers also consist of 4 dipole magnets, two-time projection chambers, and three drift chamber packages[30]
- PHOBOS is one of four detectors at RHIC used to study nucleon-nucleon collisions with the center of mass energies of 130 GeV. The effort was to detect almost all produced charged particles with almost complete coverage of the solid angle in the range of transverse momentum and pseudorapidity, focusing on particles near mid-rapidity $0 \leq \eta \leq 2$. The detector included two spectrometers for the analysis of produced particles with low transverse momentum $p_T < 1$ GeV/c. With the use of a silicon pad, it was possible to track particles, locate the vertex and measure the particle multiplicity[31]
- PHENIX is a detector to study the spin of protons and the properties of a new state of matter under extreme conditions called quark-gluon plasma in nucleon-nucleon, proton-proton, and proton-nucleon collisions. It was the largest experiment of four at RHIC. The detector measures di-lepton pairs (electrons and muons) and hadrons produced in collisions with the help of a global detector used to characterize particles and two central spectrometers at mid-rapidity to measure hadrons, photons, and electrons and another pair of forward spectrometers to measure muons with excellent resolution energy and momentum. Currently, the experiment is no longer running and the sPHENIX experiment has become its successor[32]
- sPHENIX is a new upgrade to the PHENIX detector, with several new parts to be added to the detector, which should start collecting data in 2023.[33] One of the new features is inner and outer calorimeters for particle properties measurements and cylindrical superconducting magnets at the core of the detector. While bending the trajectories of the particles created in the collisions,

the magnet will allow to differ between particles that come in three different mass states. It will enable a better study of matter and binding forces binding quarks and gluons into larger particles[34]

- STAR detector will be discussed further in the next section

2.3 STAR experiment at RHIC

The Solenoidal Tracker at RHIC (STAR) together with the sPHENIX detector, is one of two operating detectors at RHIC. The detector is primarily used to study the production of hadrons and quark-gluon plasma formation during the collisions of protons and ions, thus enabling an understanding of the state of the universe seconds after its creation during the Big Bang. During the collisions of protons, ions or pomerons of high energies particles interact through strong or electromagnetic interaction (UPCs). High-density Quantum Chromodynamics (QCD) or parton distribution function from proton-proton and proton-nucleus interactions are also being studied utilizing a system of detectors, each specializing in detecting certain types or characterization of particles, for accurate tracking, momentum measurement, identification of particles, and localization of primary vertexes from collisions or secondary vertexes from decay or particle interaction that STAR has. STAR can also provide insight into the spin orientation of individual gluons and their contribution to the spin of polarized protons.[7] The view of the STAR detector is shown in Figure 2.4 and Figure 2.5.

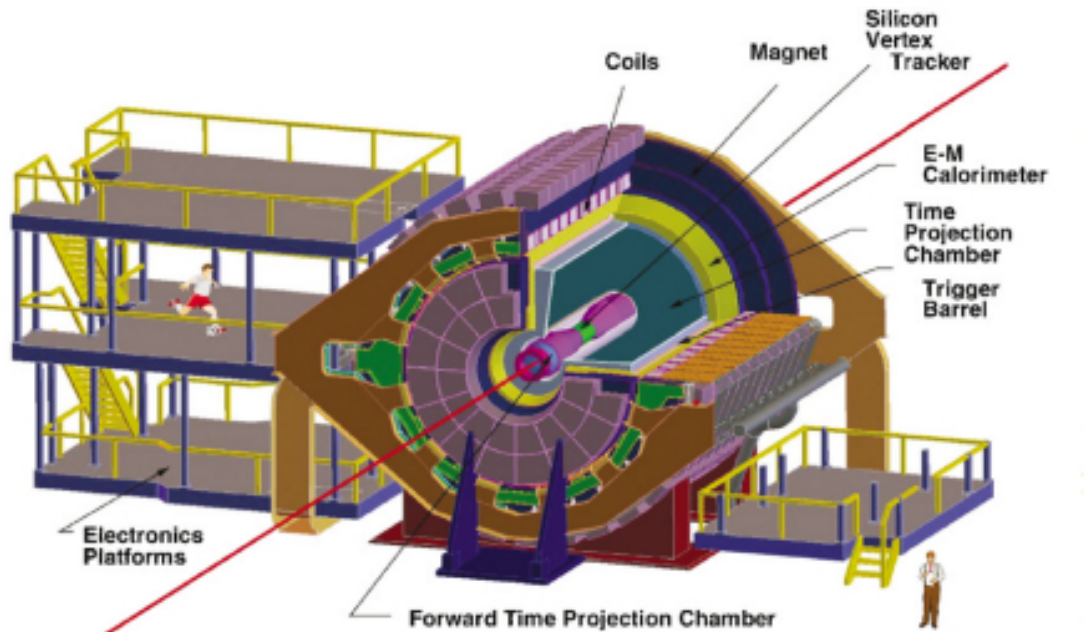


Figure 2.4: Perspective view of the STAR detector, with a cutaway for inner detector system[7].

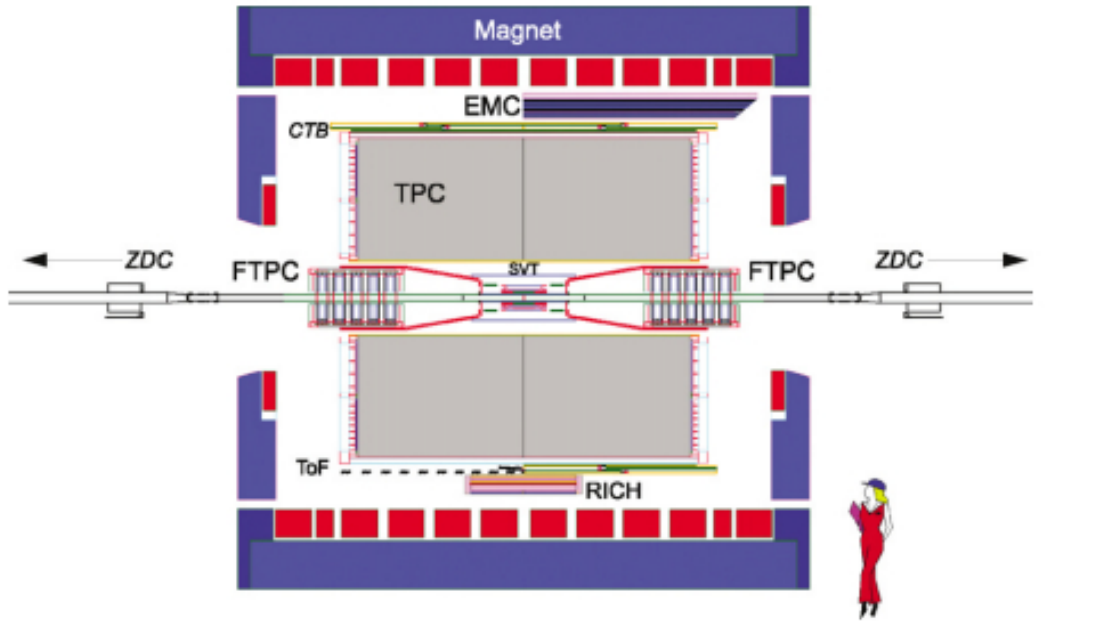


Figure 2.5: Cutaway side view of the STAR detector as configured in 2001 [7].

In the following section, we will describe the individual parts of the detector.

The largest part of the STAR detector, weighing 1100 tons, is a large room temperature solenoidal magnet of cylindrical structure located along the axis of the beam z with dimensions of 7.32 m in diameter and 7.25 m in length. The magnet is the source of a uniform magnetic field with a maximum value of 0.5 T, curving the path of charged particles provides momentum analysis covering the entire TPC volume.[35]

A large volume Time Projection Chamber (TPC) is a central element of the detector that surrounds the interaction vertex and is used for particle identification and tracking using particle ionization energy loss. It is an empty volume of P10 gas (10% methane, 90% argon) with an electric field ≈ 135 V/cm defined by the central membrane (CM) with a voltage of 28 kV for electrons to drift. TPC is 4.2 m long and 4 m in diameter with $z = 0$ at the center of TPC with radial distance from 50 to 200 from the beam axis, acceptance covers pseudorapidity of range $|\eta| < 1.8$ for tracking with complete azimuthal symmetry $\Delta\phi = 2\pi$. Particles ionizing the gas volume through which it passes are reconstructed with high precisions from secondary electrons drifting to the readout, where particles are detected by the system based on Multi-Wire Proportional Chambers (MWPC) with readout pads providing the amplification of 1000 to 3000. A number of drifting electrons and their diffusion defines the position resolution.[36]

Cherenkov detector was installed to improve the measurement of STAR rest measurement of ionization in the tracking detector during the identification of individual particles in mid rapidity in the interaction at a large value of the transferred momentum. The production of particles in high transverse momentum collisions is described by perturbative QCD and depends on the state of the hot dense nuclear matter produced in the collision. A detector is covering a region $|\eta| < 0.3$ and azimuthal angle of $\Delta\phi = 0.11\pi$, providing a reconstruction of two-dimensional information of the position of the Cherenkov photons. In combination with MWPC localization of photon-electron and charged particle is possible. The detector has produced an anti-proton to proton ratio at mid-rapidity for 130 GeV per nucleon Au-Au collisions for a range of transverse momentum $2.0 < p_T < 2.5$ GeV/c.[37]

The Time of Flight (TOF) detector based on a Multi-gap Resistive Plate Chamber (MRPC) is the barrel detector for increasing the possibility of identification and measurement of particles and obtaining the maximum amount of information on an event-by-event basis in collisions of heavy ions with high acceptance. TOF acceptance covering the whole azimuthal angle $\Delta\phi = 2\pi$ range and $|\eta| < 1$ in pseudorapidity matching the acceptance of TPC. The MRPC detector shown in Figure 2.6 is capable of a time resolution below a hundred picoseconds and high detection efficiency for Minimum Ionizing Particles (MIP). Approximately 3800 MRPC modules, each with six pairs of copper pick-up pads, are required to cover the STAR detector area. The measurement system of the TOF detector is based on the time interval, the time of arrival of the particle to the MRPC detector, the time is related to the reconstructed tracks and the total time interval resolution of 100 ps. MRPCs are a form of stacked resistive plates with a series of uniform gas gaps with a strong electric field, which is created by the voltage applied to the electrodes on the outer surface of the plates with pickup pad layers separated from the electrodes by Mylar. Subsequently, particles passing through the chamber create an avalanche in gas gaps.[8] Particle identification in the STAR experiment is illustrated in Figure 2.7. Electron identification involves TPC and the TOF detector, by combining them, a better measurement of electron identification is achieved.[9]

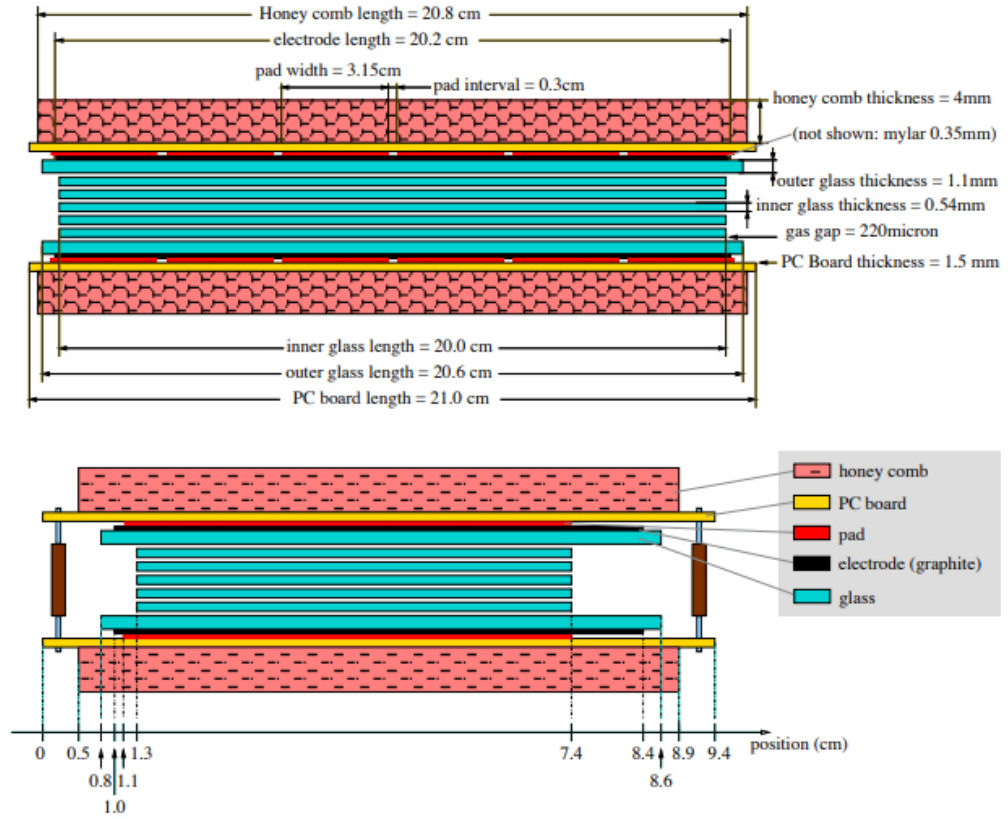


Figure 2.6: Two side views on the structure of an MRPC module [8].

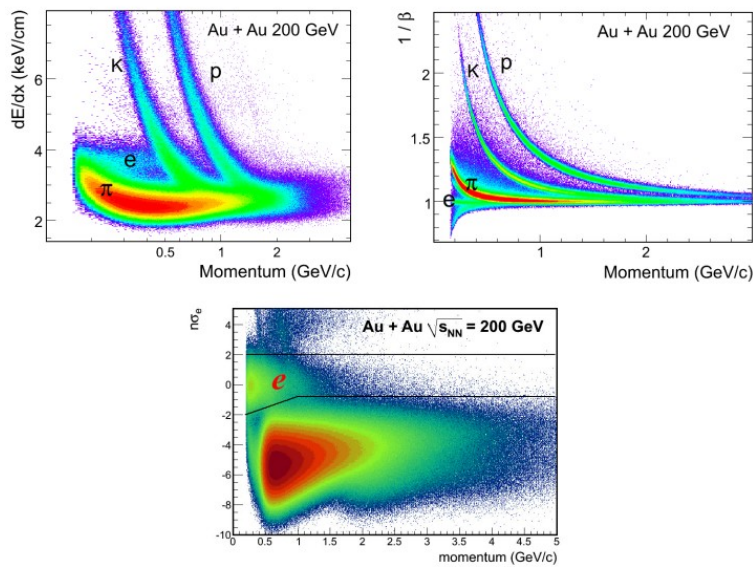


Figure 2.7: Measurement in TPC detector of energy-loss dE/dx (upper left figure), $1/\beta^2$ measurement in TOF detector (upper right figure) and improved electron identification by combining the TOF and TPC measurements (lower figure) [9].

Barrel Electromagnetic Calorimeter (BEMC) shown in Figure 2.8 is a sampling scintillator-lead calorimeter located within the STAR magnet at a radius of ~ 220 cm just outside the TPC. BEMC is composed of 120 modules, each module is a stack of 21 scintillator mega tiles separated by 5 mm lead sheets, the light signal from 21 scintillators is collected at a single phototube. BEMC has the pseudorapidity coverage of $|\eta| < 1$ covering the whole azimuthal angle $\Delta\phi = 2\pi$. [10]

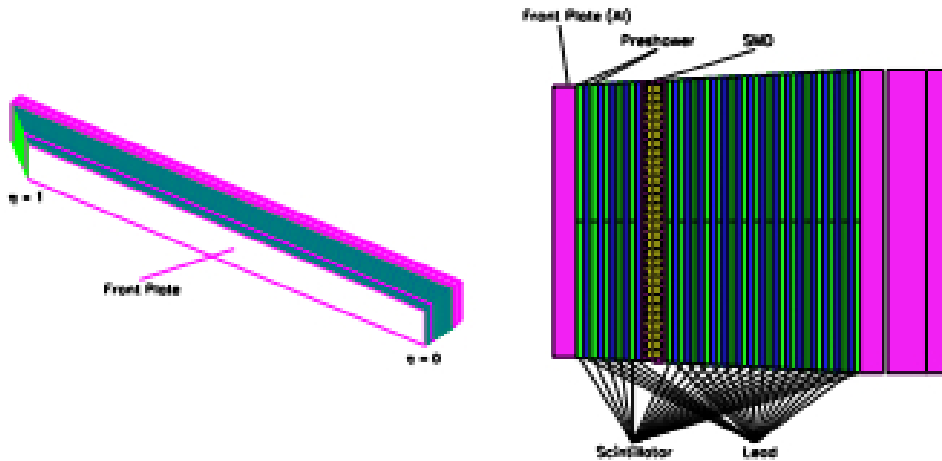


Figure 2.8: BEMC module (left) with its cross section (right) [10].

Endcap Electromagnetic calorimeter (EEMC) enables measurement of transverse energy and high transverse momentum of photons, electrons, and hadrons decaying electromagnetically adding coverage for asymmetric partonic collisions. EEMC covers pseudorapidity values $1 < \eta \leq 2$ and the full azimuthal angle $\Delta\phi = 2\pi$ implementing BEMC. Shower-maximum detectors are also included to distinguish high-momentum single photons from photon pairs resulting from meson decays. [38]

Beam-Beam Counter (BBC) is a set of scintillator annuli around RHIC beam pipe on the east and west pole tips of the STAR magnet located at 3.75 m from the center of the STAR interaction region. Each of the two annuli consists of packed hexagonal detectors in the inner and outer rings. The inner ring has 6 tiles and the outer ring has 12 tiles. The scintillation signal is transmitted to the photomultiplier by optical fibers inserted in each tile. An average signal of 15 photoelectrons is obtained for a MIP. BBC covers a range of pseudorapidity of $3.4 < \eta \leq 5.0$. [39]

Zero-Degree Calorimeters (ZDC) are very forward with a range of pseudorapidity $|\eta| > 6.6$ [4]. Detectors located 18 m from the center of the STAR detector between RHIC beam pipes (ZDC-E for the east detector and ZDC-W for the west detector) behind the dipole magnets bending trajectories of charged particles, leaving only neutral particles to hit the ZDC. The purpose of the detectors is to detect

and measure the energy in the forward direction of uncharged particles (neutrons) escaping from the interaction region. ZDC is also useful in luminosity measurement, as a trigger, determination of collision centrality, or as charged particle multiplicity correction in TPC. The neutron multiplicity is obtained from the total energy measurement. The ZDC on each side of the STAR detector has 3 identical modules and a shower maximum detector on each side recording neutron beam position information. ZDC modules consist of tungsten plates, fibers, and photon multiplier tubes.[11]

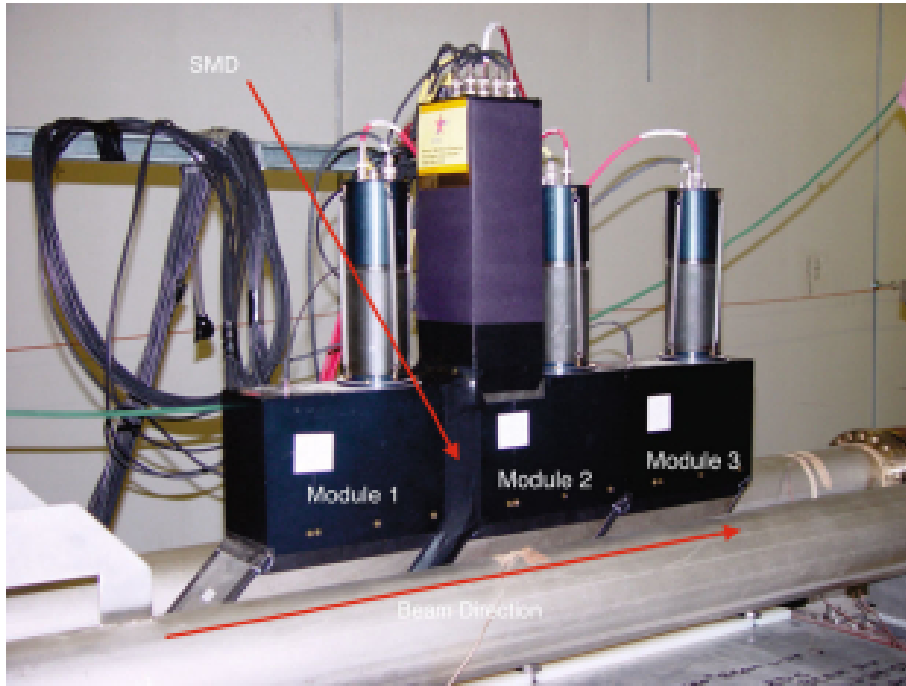


Figure 2.9: ZDC modules installed on STAR experiment [11].

Event Plane Detector (EPD) is located at a distance of 3.75 m from the center of the STAR detector and is used for the determination of the initial geometry of individual collisions measuring charged particles emitted in the forward and backward directions from collisions, covering pseudorapidity region $2.14 < \eta \leq 5.09$. EPD consists of two wheels, each wheel composed of 12 supersectors, which are further divided into 31 tiles. Each tile is connected to an optical fiber transmitting light to a silicon photomultiplier (SiMP).[40]

Muon Telescope Detector (MTD) was installed between 2012 and 2014 at a radius of 403 cm. MTD is a fast detector to record hits generated by charged particles and provides single-muon and dimuon triggers based on the number of hits. the detector covers an azimuthal angle of 45% and a pseudorapidity of range $|\eta| < 0.5$.[41]

Vertex Position Detector (VPD) is integrated into the STAR trigger system and provides the primary detector input to minimum-bias trigger in Au+Au collisions. The system consists of two identical assemblies, each assembly contains nineteen detectors on both sides of STAR. Each detector is composed of a PB converter and plastic scintillator with a photomultiplier tube serving as a readout. The detector covers approximately half of the solid angle in the pseudorapidity range of $4.24 < \eta \leq 5.1$. [42]

Forward Calorimeter System (FCS) which has undergone a recent forward upgrade of STAR detector to investigate QCD physics for very high and low values of Bjorken's x as well as to improve the ability to probe longitudinal structure and the temperature dependence of heavy ion collision properties. FCS is driven by detector performance. Calorimeters have a good resolution of hadronic and electromagnetic energy covering the range of pseudorapidity $2.5 < \eta \leq 4$. The FCS design consists of a pre-shower and post-shower detector, a Spaghetti ElectroMagnetic Calorimeter (SPACal), made of Tungsten powder and scintillating fibers, followed by a Lead and Scintillating Plate sampling Hadronic Calorimeter (HCal). The reconstructed PHENIX sampling ECal [43] is also part of the FCS. FCS system has very good electromagnetic and hadronic energy resolutions with both calorimeters HCal and ECal, installed in 2020, having the same readout electronics and photo sensors SiPMs and Avalanche Photodiode (APD). [12]

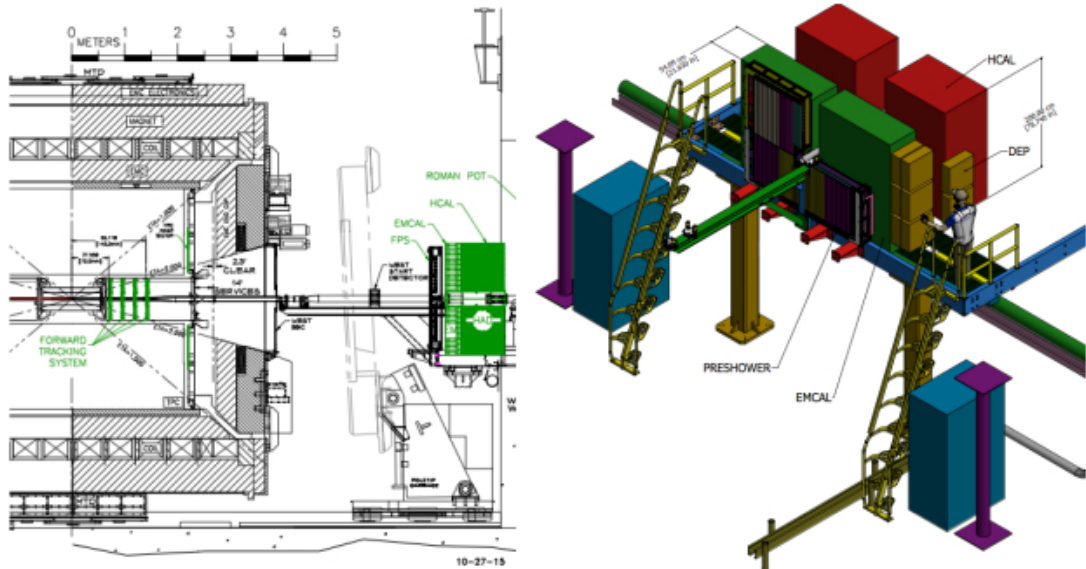


Figure 2.10: Location of the FCS at the west side of the STAR experiment and a three-dimensional CAD model of the FCS [12].

Forward Tracking System (FTS) aided by the 0.5 T magnetic field is also an addition to the FCS for splitting electrons and positrons, resolving the hadron charge sign and measuring the transverse momentum of charged particles in the range $0.2 < p_T \leq 2$ GeV/c in heavy ion collisions. The FTS consists of 3 silicon disks at a

distance of 140-180 cm from the center of the detector to cover the pseudorapidity $2.5 < \eta \leq 4$. [12]

The STAR trigger system depends on fast detectors such as ZDC and Central Trigger Barrel (CTB) which consists of 240 scintillator slats covering $|\eta| < 1$ [17] and event selection for slow detectors. The CTB surrounds the outer cylinder of the TPC and triggers on the flux of charged particles in the midrapidity region. The data Acquisition system (DAQ) is fast and flexible with an event size of order 200 MB and the events are processed at input rates up to 100 Hz. [7]

Chapter 3

Observation of J/ψ in UPCs and structure of interaction points

The theoretical part of this work consisted in getting to know the method of processing the measured data in the ultra-peripheral collisions of two opposing Au+Au beams at the STAR experiment at energy $\sqrt{s} = 200$ GeV per nucleon during the production of the J/ψ particle, i.e. the bound state of the quark-antiquark ($c\bar{c}$) pair, which is detected through its dielectron decay $J/\psi \rightarrow e^+e^-$. Subsequently, also the examination of particular structure of interaction points along the beam axis on ZDC vertices from a UPC trigger. The data used in the processing came from Run 14 Au+Au on the STAR experiment covering the period from 25 March 2014 to 16 June of the same year. The first part of this chapter is devoted to describing the physical quantities used to describe the collisions of the opposite beams in the accelerator. The next part is the data processing itself.

3.1 Physical quantities for particle collisions description

Information for this section is taken from [14] and [13]. Collisions of particles in accelerators occur at high energies, higher than the rest energy of the particles in the collision and at speeds close to the speed of light, and therefore it is necessary to approach the description using the special theory of relativity and four-vectors (in covariant form) $x^0 = ct$, $x^1 = x$, $x^2 = y$, $x^3 = z$. We will also consider the so-called system of natural units, therefore $\hbar = c = 1$. The transformation between inertial systems that move at a mutual velocity v is done by using the Lorentz transformation and the relativistic factor $\gamma = \frac{1}{\sqrt{1-v^2}}$, where $v \in (0, 1)$. We are primarily interested in quantities that are invariant to a change in the coordinate system, that is, i.e. quantities that do not change during transformation.

When describing collision processes, the center of mass coordinate system associated with the center of gravity, which is at rest, is most often used. We are interested in the relative motion of the particles and the total momentum of the system is zero. The z-axis is parallel to the direction of movement of the beam and the x,y axes form a plane perpendicular to the direction of movement of the beam. Quantities such as position and momentum can be divided into components parallel to the direction of motion $x_{||}$, $p_{||}$ and components perpendicular to the motion x_{\perp} , p_{\perp} . Perpendicular components do not change during the transformation.

Invariant mass

One of the main relativistic invariants is the square of the four-momentum $p = (E, \vec{p})$ and thus

$$p^2 = E^2 - \vec{p}^2 = m^2. \quad (3.1)$$

This relativistic invariant is called invariant mass.

The square of the invariant mass for a system of particles is usually denoted by s

$$s = E^2 - p^2 \geq 0. \quad (3.2)$$

In the center of mass system, also applies: $\sum \vec{p}_i = 0$ and for n particles then

$$s = \left(\sum_{i=1}^n \tilde{E}_i \right)^2 \quad (3.3)$$

is the square of the total energy in the center of mass system.

If we consider only 2 particles

$$\left(\tilde{E}_1 + \tilde{E}_2 \right)^2 = s = (E_1 + E_2)^2 - (\vec{p}_1 + \vec{p}_2)^2. \quad (3.4)$$

The square of the total energy in the center-of-mass system s is also called the Mandelstam variable, which is Lorentz invariant.

Longitudinal and transverse momentum

If we consider the direction of the beam axis along the z-axis, then the momentum components perpendicular to the direction of movement do not change during the transformation and we can define the longitudinal momentum: $p_L = p_{||} = p_z$, which undergoes a Lorentz transformation and the transverse momentum $p_T = p_{\perp} = \sqrt{p_x^2 + p_y^2}$. Using the relation for transverse momentum, we can also define the transverse mass as[14]

$$m_{\perp} = \sqrt{m^2 + p_T^2}. \quad (3.5)$$

Rapidity

Rapidity is an expression of relativistic longitudinal velocity, which at low values turns into velocity itself. It is one of the most important high-energy quantities, defined as[13]

$$y = \frac{1}{2} \ln \left(\frac{E + p_L}{E - p_L} \right), \quad (3.6)$$

where E is the energy of the particle and p_L is the longitudinal momentum. However, the rapidity is not invariant to the Lorentz transformation but is transformed using the relation

$$\tilde{y} = y - \frac{1}{2} \ln \left(\frac{1 + \beta}{1 - \beta} \right). \quad (3.7)$$

Rapidity can be divided into several regions. The region around the center of the distribution is called the mid-rapidity region, in the center of mass system it is the region around $y = 0$. The region of large positive rapidities is the forward rapidity region and the region of small or negative rapidities is the backward rapidity region.

Pseudorapidity

For highly relativistic particles, the energy and the total momentum are often difficult to measure, especially at high values of rapidity. Pseudorapidity, an approximation to rapidity can be used when the rest mass of the particles can be neglected. Pseudorapidity depends on only one variable, the angle θ , and is defined as

$$\eta = -\ln \left(\tan \frac{\theta}{2} \right), \quad (3.8)$$

where θ is the angle between the momentum of the particle \vec{p} and the axis of the beam.

For large values of momentum, η and y coincide.

Interaction rate and luminosity

We will now also introduce the interaction rate, which indicates the number of interactions per second defined as

$$R_{int} = L \frac{d\sigma}{d\Omega} (\theta, \psi), \quad (3.9)$$

where $\frac{d\sigma}{d\Omega} (\theta, \psi)$ is differential cross section, θ is scattering angle and ψ is azimuthal angle.

$L [m^{-2}s^{-1}]$ is a quantity called luminosity, which does not depend on the type of interaction but only on the properties of the bundles in the accelerator. Luminosity is given by[13]

$$L = f \frac{N_1 N_2}{S}, \quad (3.10)$$

where f is the collision frequency, S is the cross-sectional area of the beam and $N_{1,2}$ is number of particles in beam.

We can also define related integrated luminosity, which is the total luminosity over a period of time

$$\mathcal{L} = \int_{t_1}^{t_2} L dt. \quad (3.11)$$

3.2 Data analysis of J/ψ in Au+Au at $\sqrt{s} = 200$ GeV

As already mentioned at the beginning of the chapter, part of this work was familiarization with the method of data processing from J/ψ photoproduction in Au+Au collisions at $\sqrt{s} = 200$ GeV at the STAR experiment.

In the first part, I will focus on the data format and their processing in the production of the J/ψ particle in UPCs, followed by the study of the particular structure of z vertices (interaction points) along the beam axis and the simulation of colliding beams for vertex distribution. All sections will also contain parts of code for analysis and graph creation.

3.2.1 Data format

Data from the STAR experiment used in the analysis are stored in star-upc-data format for UPCs analysis. Data from the original muDST were converted to UPC trees and specific selection criteria for tracks and events were applied. Data for J/ψ photoproduction or Monte Carlo (MC) templates are provided by STARLIGHT, a Monte Carlo event generator that simulates two-photon and photon-Pomeron interactions between relativistic nuclei and protons. Starlight is able to model coherent and incoherent vector mesons production for photonuclear interactions.[44] Events of coherent J/ψ in dielectron decays are simulated via the full STAR geometry. Event of incoherent J/ψ from two-photon production of dielectron pair $\gamma\gamma \rightarrow e^+e^-$ are also generated by the Starlight generator.

The requirement for the coherent J/ψ production was the emission of at least one neutron by each nucleus in the forward direction. The emission of a neutron is provided by nOOn event generator in the process of J/ψ photoproduction. The nOOn is a Monte Carlo ROOT-based program, which adds the neutrons to e^+e^- pairs from J/ψ decay from Starlight. The generator provides a text file with transverse momentum p_T and mass, which are filled into the TTree dataset by making a C structure and addressing variables.[45]

As mentioned in the introduction of this chapter, processed data came from Run 14 Au+Au on the STAR experiment covering the period from 25 March 2014 to 16 June 2014.

I processed the provided data files in PyROOT, which stands for using ROOT from Python. For processing, I used the school computer Sunrise[46], to which I connected from my personal computer using the program MobaXterm.

3.2.2 Trigger requirement and data selection

The data I worked with was already the result of trigger requirements for the J/ψ sample UPCJpsiB, to which the selection criteria were subsequently applied to obtain a sample of J/ψ candidates and a clean sample of e^+e^- pairs.

Requirement for the main trigger for the J/ψ sample UPCJpsiB:

- Two tracks and at least one neutron in each ZDC. Neutrons are a convenient way to tag UPC events at the trigger level.
- Limited activity in TOF (2-6 hits).
- Back-to-back activity in BEMC.

Furthermore, selection criteria are put on the UPCJpsiB sample.

Requirements for tracks:[47]

- Track is matched to a fired BEMC cluster.
- Track has at least 14 hits in TPC.
- Track pseudorapidity is $|\eta| < 1$.
- Veto from both BBC small tiles for central hadronic collision rejection.

Requirements for events:

- Only one pair is formed by 2 good tracks already from the same vertex, when the dielectron pair is emitted out of the interaction region, each electron moving in the opposite direction.
- Tracks opening angle at BEMC is $\Delta\phi_{BEMC} > 2.618$ from back-to-back trigger requirement.
- Dielectrons satisfy particle identification for both tracks.
- Position of primary vertex along the z direction is $|z_{vertex}| < 100$ cm.
- Rapidity y of J/ψ candidate is $|y| < 1.0$.
- Tracks in the pair are of the unlike sign.

As mentioned in 3.2.1, the signal consists of the coherent and incoherent signal of J/ψ and contribution from $\gamma\gamma \rightarrow e^+e^-$. To fit data for a coherent J/ψ signal, the Crystal Ball function and the empiric formula for the two-photon dielectron background are used. Contribution from $\gamma\gamma \rightarrow e^+e^-$ is normalized using fit to the invariant mass distribution. To separate incoherent and coherent components of the signal, fit to transverse momentum in $\log_{10}(p_T)^2$ is used. Cross section of J/ψ photoproduction in Au+Au at 200 GeV with neutron emission is calculated as a function of $|t|$, where $|t| = p_T^2$. In this work, however, we will not focus on data separation and cross section calculation.[48]

3.2.3 Data processing for J/ψ

In this subsection, plots created from the data described in subsection 3.2.1 will be presented. The selection rules described in subsection 3.2.2 have already been applied to the data. At the same time, here and in the following subsections dedicated to data processing, I will present parts of the code used to create individual plots that refer to the final stage of reconstruction. The number of events for a range of values of mass $m_{e^+e^-}$, transverse momentum p_T , and rapidity y of the dielectron pair, which is used to detect J/ψ from its decay $J/\psi \rightarrow e^+e^-$, are displayed in the histograms below along with the values of mean value, standard deviation, and number of entries, which are shown as part of histograms. The electron identification for the results involves the TPC and the TOF detector.[9]

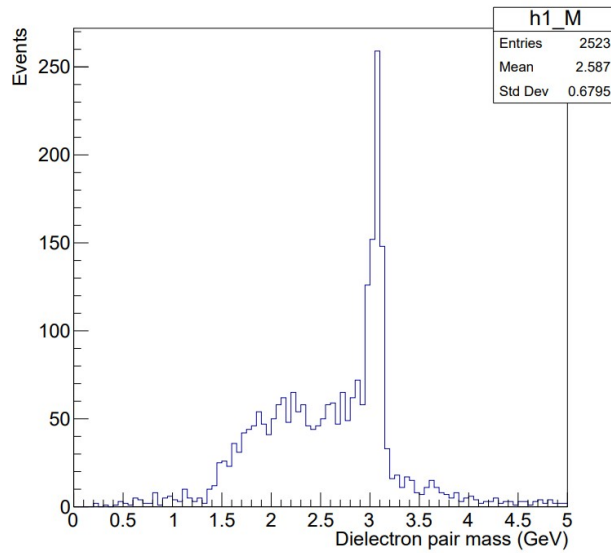


Figure 3.1: Mass of dielectron pair e^+e^-

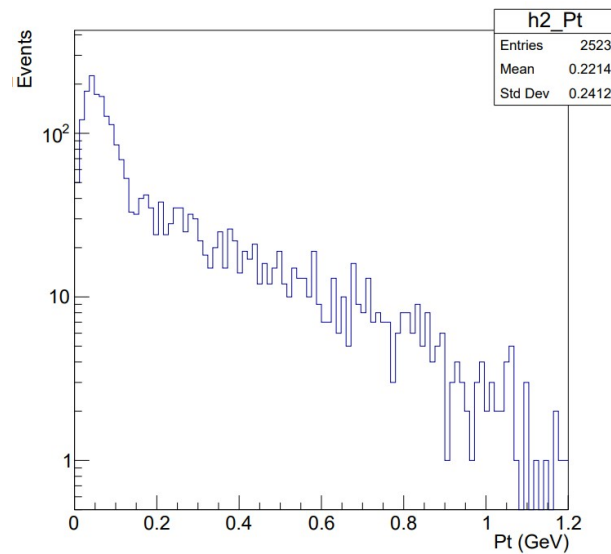


Figure 3.2: Transverse momentum of dielectron pair e^+e^-

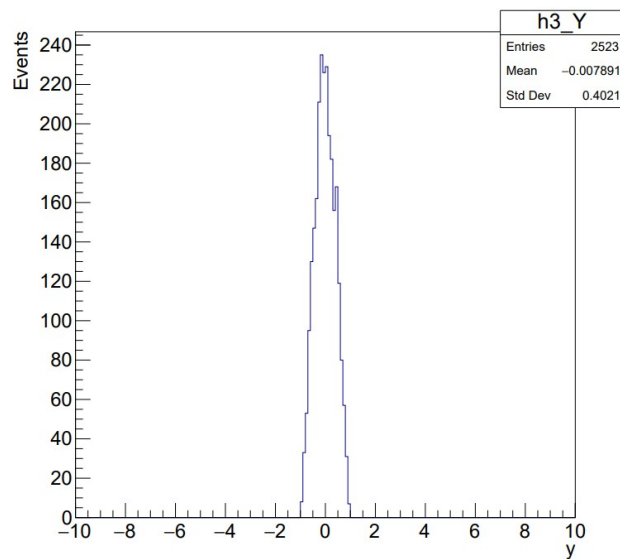


Figure 3.3: Tracks rapidity

The first step to creating the graphs was to open the file and get the tree in which the data was stored.

```

1 #!/cvmfs/sft.cern.ch/Lcg/views/LCG_98python3/x86_64-centos7-gcc8-opt/bin/python3
2
3 from ROOT import TFile, TCanvas, TH1D
4 inp = TFile.Open("ana_muDst_run1_all_sel5z.root")
5 tree = inp.Get("jRecTree")

```

Figure 3.4: Part of code to open the file and get the tree with data.

I then created a histogram that I filled with data.

```

8
9 h1_M = TH1D("h1_M", "h1_M", 100, 0, 5)
10
11 tree.Draw("jRecM >> h1_M")

```

Figure 3.5: Filling a histogram with data.

The plot shows the number of events on a large range of individual variables. By adding additional conditions to the data, I restricted myself to the region of the peaks and thus to regions corresponding to J/ψ . The restrictions were on the mass of the dielectron pair to correspond to J/ψ particle mass interval, at (2.6, 3.4). Next is the limitation on the rapidity interval (Subsection 3.2.2) $|y| < 1$ and the transverse momentum $p_T < 0.2$ GeV, that is, to a low value of p_T for the signal of coherent J/ψ . Histograms with additional restrictions are shown in Figures 3.6, 3.2, and 3.8 again with values of mean value, standard deviation, and number of entries.

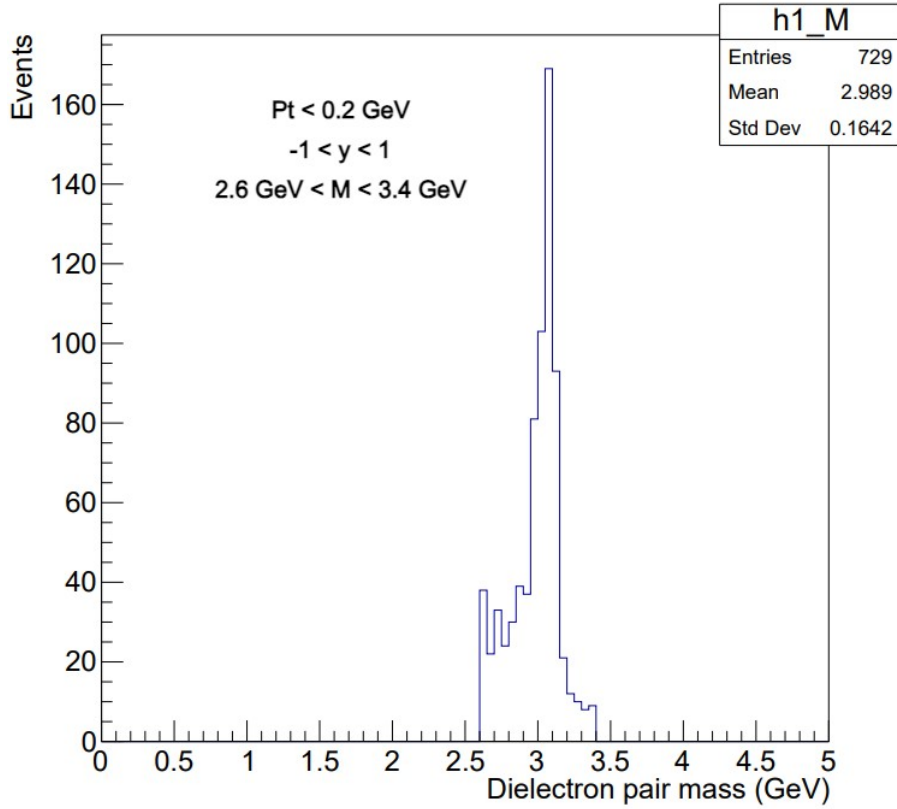


Figure 3.6: Mass of dielectron pair e^+e^- after restriction.

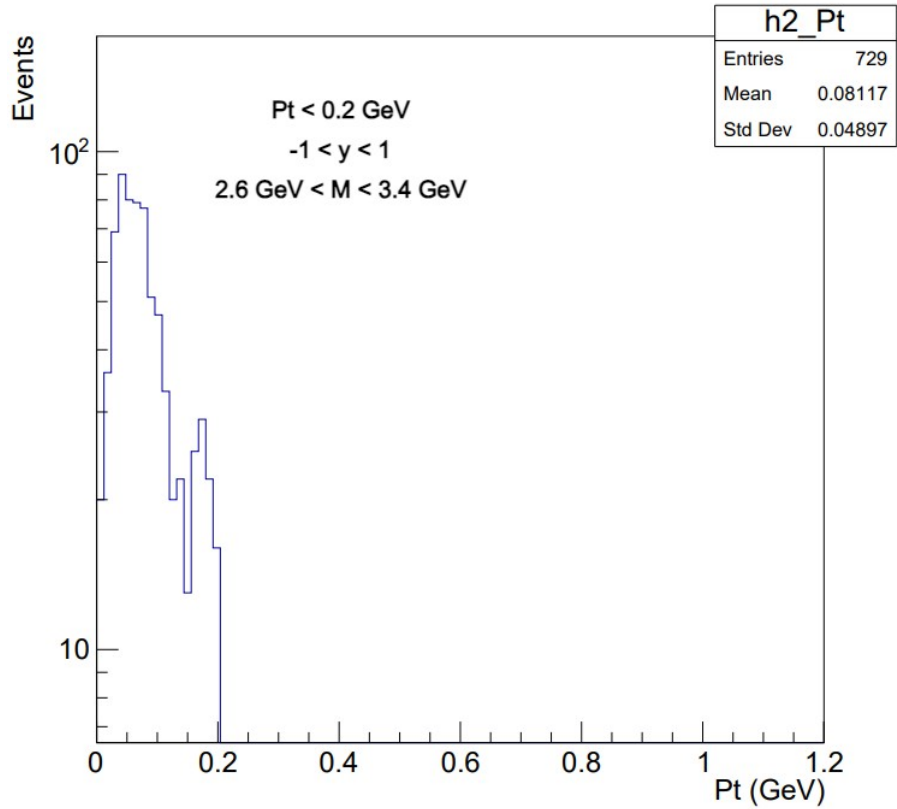


Figure 3.7: Transverse momentum of dielectron pair e^+e^- after restriction.

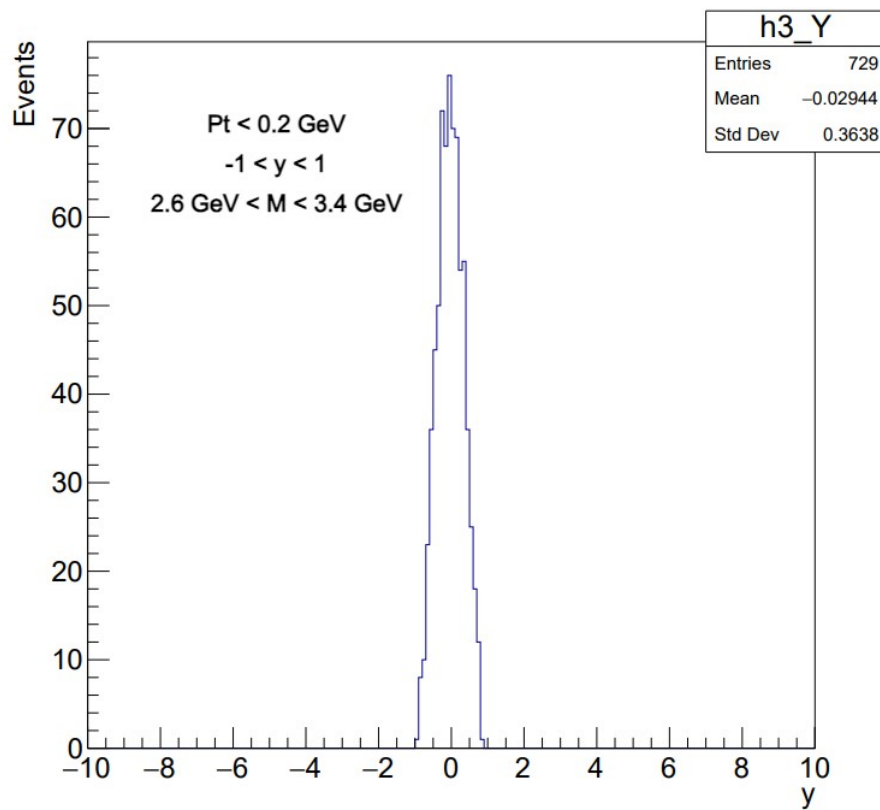


Figure 3.8: Tracks rapidity after restriction.

This was done simply by adding a line of code for additional conditions to the data, shown in Figure 3.9.

```
10 tree.Draw("jRecM >> h1_M", "jRecPt < 0.2 && jRecM > 2.6 && jRecM < 3.4 && jRecY < 1 && jRecY > -1")  
11
```

Figure 3.9: Restrictions to data.

3.2.4 Position of ZDC vertex

In this subsection, a plot of the position of the interaction points along the axis of beam z - z vertices are presented. The position of the z -vertices is determined by forward ZDC detectors, that detect neutrons emitted by nuclei, as one of the trigger requirements for the coherent J/ψ production was the emission of at least one neutron by each nucleus in the forward direction (Subsection 3.2.2). Neutrons are a good way for tagging UPC events. The z -vertex distribution is shown in Figure 3.10.

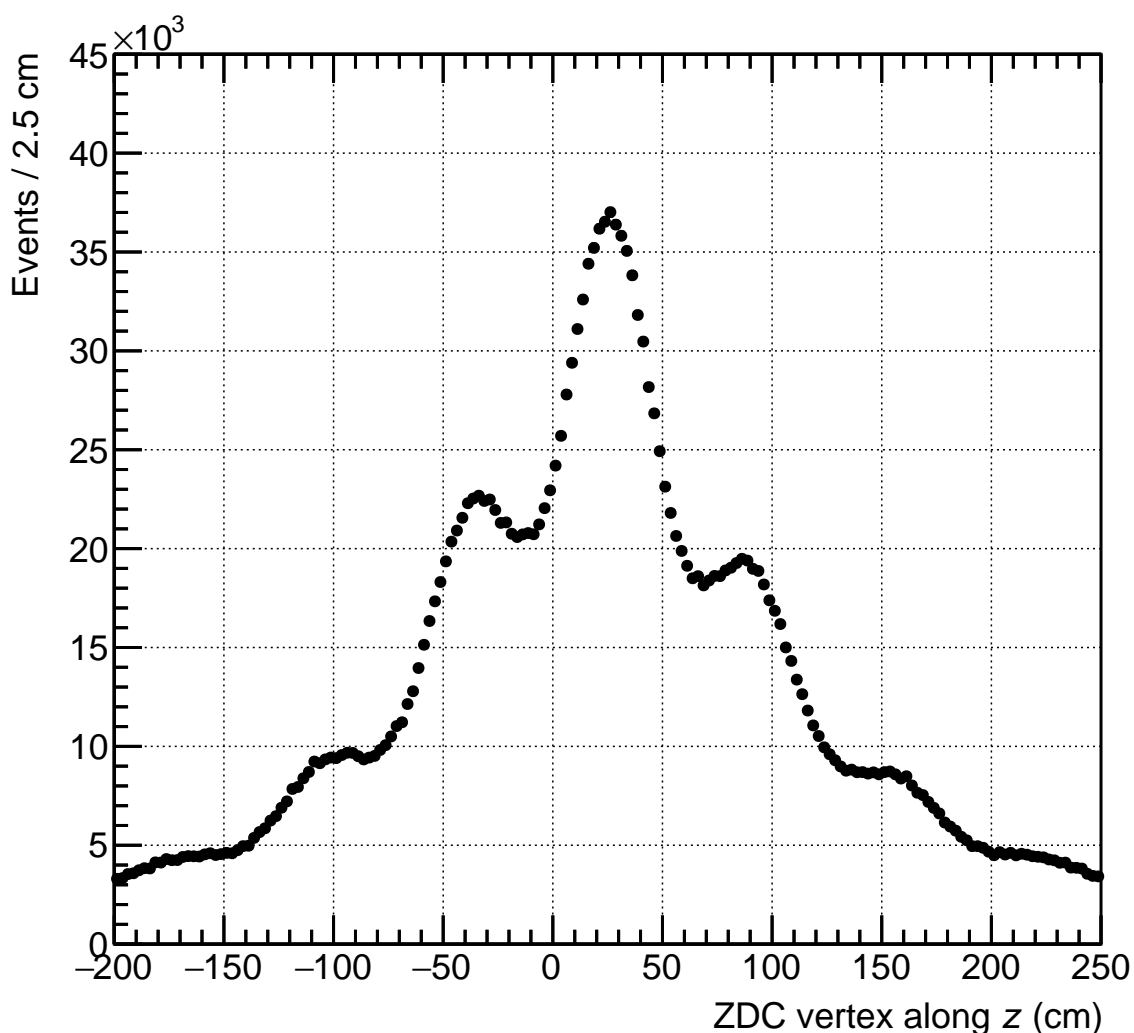


Figure 3.10: z -vertex distribution along the beam axis.

In Figure 3.11 and Figure 3.12 parts of the code to plot the z -vertex distribution from Figure 3.10 are shown.


```

1 #!/cvmfs/sft.cern.ch/lcg/views/LCG_98python3/x86_64-centos7-gcc8-opt/bin/python3
2
3
4 import ROOT as rt
5 import math
6 from ROOT import gPad, gROOT, gStyle, TFile, gSystem, TH1D, TCanvas, TArrow, TLine, TText, TLatex
7 from ROOT import RooRealVar, RooDataSet, RooArgSet, RooArgList, RooDataHist
8 from ROOT import RooGaussian, RooAddPdf
9 from ROOT import RooFit as rf
10
11 import sys
12 sys.path.append('/home/adamjaro/star-upc-data/ana/muDst/muDst_run1/sel5/ana_muDst_run1_all_sel5.root')
13 import plot_utils as ut
14 from parameter_descriptor import parameter_descriptor as pdesc
15
16
17 if __name__ == "__main__":
18
19     basedir = "/home/adamjaro/star-upc-data/ana/muDst/muDst_run1/sel5/ana_muDst_run1_all_sel5"
20     infile = "ana_muDst_run1_all_sel5.root"
21
22     binned = True
23     fitran = [-130, 200]
24
25     vbin = 2.5
26     vmin = -200
27     vmax = 250

```

Figure 3.11: Part of code for used classes imported from ROOT, getting data from a dataset and determining bins (maximum, minimum, and bin size).

```

48
49     loglist1 = [(x,eval(x)) for x in ["infile", "vbin", "vmin", "vmax"]]
50     loglist2 = [(x,eval(x)) for x in ["fitran", "binned", "f_4s"]]
51     strlog = ut.make_log_string(loglist1, loglist2)
52     ut.log_results(out, strlog+"\n")
53
54
55     nbins, vmax = ut.get_nbins(vbin, vmin, vmax)
56     z = RooRealVar("jZDCVtxZ", "z", vmin, vmax)
57     z.setRange("fitran", fitran[0], fitran[1])
58     data = RooDataSet("data", "data", tree, RooArgSet(z))
59     hZdc = TH1D("hZdc", "hZdc", nbins, vmin, vmax)
60     tree.Draw("jZDCVtxZ >> hZdc")
61     dataH = RooDataHist("dataH", "dataH", RooArgList(z), hZdc)
62

```

Figure 3.12: Code for fit to logarithmic scale of displaying data (first part), and for data input from the tree (second part).

I then fitted the structure for the z-vertex distribution using the model of Gaussian functions to describe the shape of the distribution. A plot with a fit of all 5 Gaussians is shown in Figure 3.13. At the same time, the graph shows the parameters of individual Gaussians, i.e χ^2 of fit by the model, mean value μ and standard deviation σ with the notation *lo/hi* for Gaussians on the left/right side from the central Gaussian and 1,2 for the first and second Gaussian from the central one.

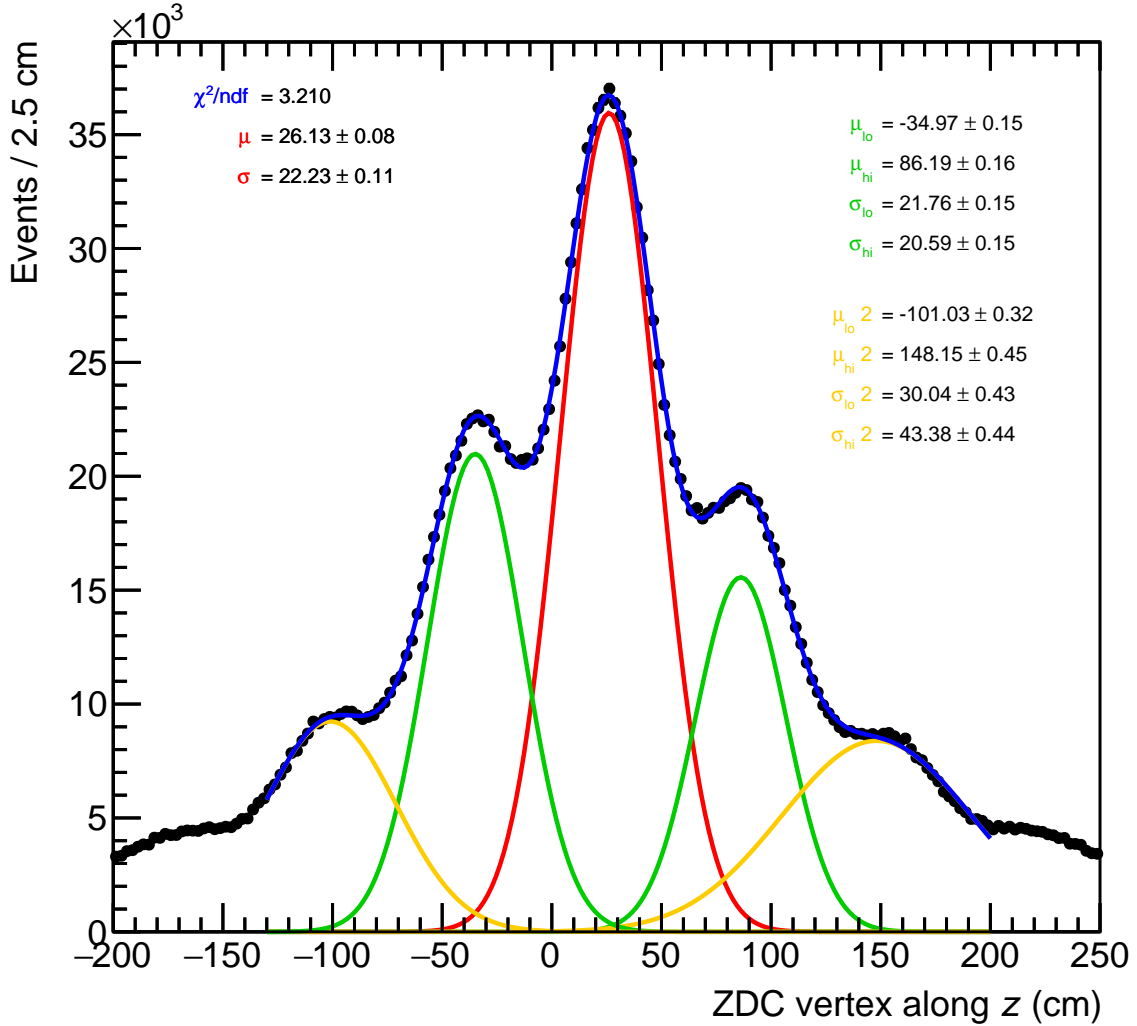


Figure 3.13: z-vertex distribution along the beam axis.

Part of the code for the model composed of 5 Gaussians is shown in Figure 3.14 and for fitting data with Gaussians in Figure 3.15.

```

78 #middle
79 m0 = RooRealVar("m0", "m0", 27, vmin, vmax)
80 sig0 = RooRealVar("sig0", "sig0", 20, vmin, vmax)
81 g0 = RooGaussian("g0", "g0", z, m0, sig0)
82
83 #first right
84 mR = RooRealVar("mR", "mR", 88, vmin, vmax)
85 sigR = RooRealVar("sigR", "sigR", 27, vmin, vmax)
86 gR = RooGaussian("gR", "gR", z, mR, sigR)
87
88 #second right
89 mR2 = RooRealVar("mR2", "mR2", 148, vmin, vmax)
90 sigR2 = RooRealVar("sigR2", "sigR2", 27, vmin, vmax)
91 gR2 = RooGaussian("gR2", "gR2", z, mR2, sigR2)
92
93 #first left
94 mL = RooRealVar("mL", "mL", -36, vmin, vmax)
95 sigL = RooRealVar("sigL", "sigL", 25, vmin, vmax)
96 gL = RooGaussian("gL", "gL", z, mL, sigL)
97
98 #second left
99 mL2 = RooRealVar("mL2", "mL2", -90, vmin, vmax)
100 sigL2 = RooRealVar("sigL2", "sigL2", 25, vmin, vmax)
101 gL2 = RooGaussian("gL2", "gL2", z, mL2, sigL2)

```

Figure 3.14: Code for 5 Gaussians used to fit the data.

```

108 ndat = data.reduce("jZDCVtxZ>{0:.3f} & jZDCVtxZ<{1:.3f}".format(fitran[0], fitran[1])).numEntries()
109 n0 = RooRealVar("n0", "n0", ndat/2.1, 0, ndat)
110 nR = RooRealVar("nR", "nR", ndat/3., 0, ndat)
111 nR2 = RooRealVar("nR2", "nR2", ndat/2., 0, ndat)
112 nL = RooRealVar("nL", "nL", ndat/2.7, 0, ndat)
113 nL2 = RooRealVar("nL2", "nL2", ndat/2., 0, ndat)
114
115 model = RooAddPdf("model", "model", RooArgList(g0, gR, gL, gL2, gR2), RooArgList(n0, nR, nL, nR2, nL2))
116
117
118
119 r1 = model.fitTo(dataH, rf.Range("fitran"), rf.Save())
120
121

```

Figure 3.15: Code for creating a model and fitting the data.

Furthermore, from the distances of the individual peaks, I determined the flight time of beam particles, moving at almost the speed of light, needed to overcome the distance. I also determined the standard deviation as the square root of the sum of the squares of the distances. I obtained the distances with the error from the parameters of individual Gaussians. The final figure containing the z-vertex distribution, fitted by the model of Gaussians with parameters and peak distance values with error is shown in Figure 3.16.

The ZDC vertices distribution from a UPC trigger, therefore, shows multiple Gaussian peaks spaced by about 2 ns. I will not include the part of the code for the arrows and vertical lines here, as it is only a stylistic element.

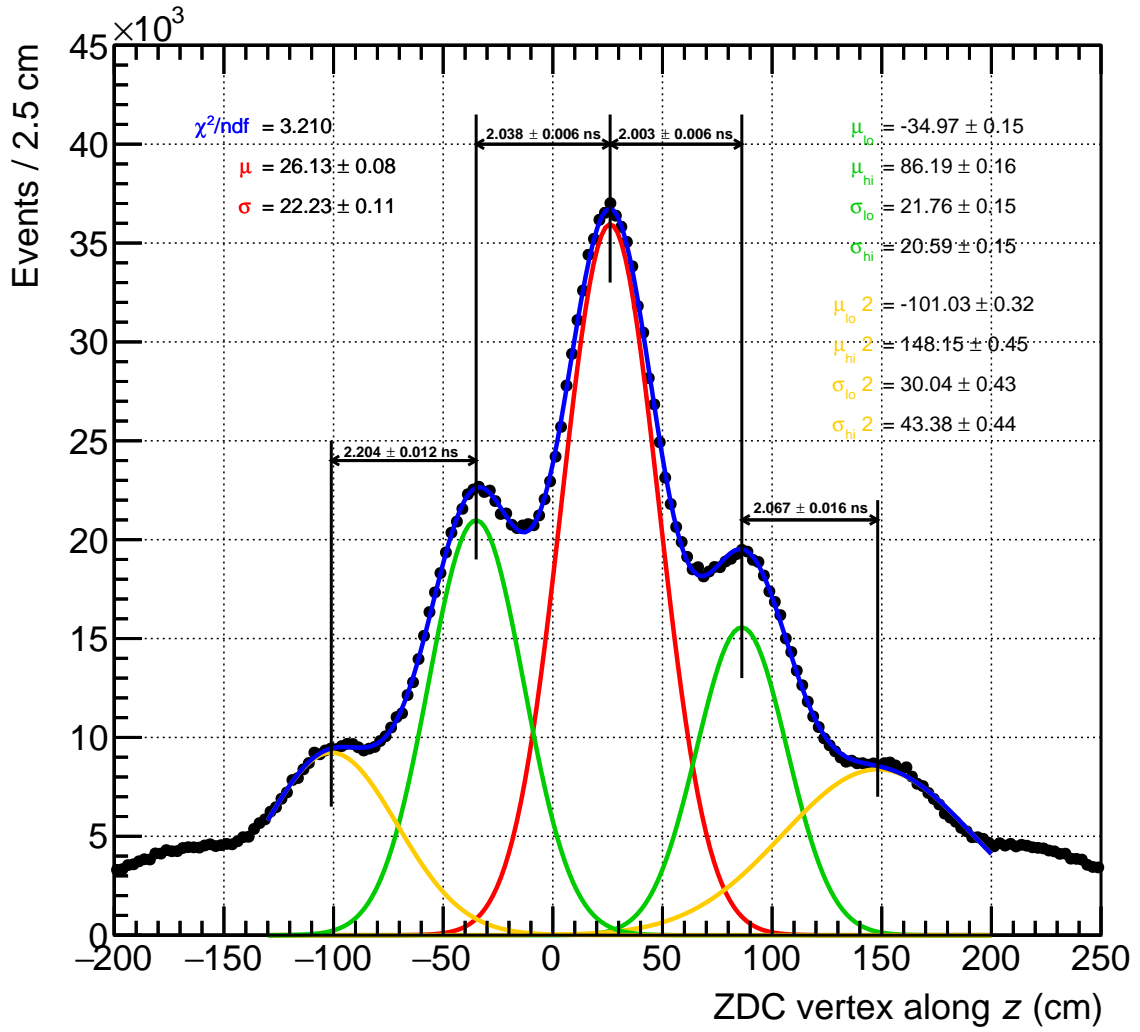


Figure 3.16: z-vertex position distribution fitted by the model of Gaussians together with the distance values between peaks.

3.2.5 Simulation of colliding beams dynamics

In this last part, I will focus on the simulation of the collision of two opposing beams of particles Au. The data used for the simulation was Wall Current Monitor (WCM)[28] data on the fill pattern for both beams (blue and yellow) from run 14 Au+Au at $\sqrt{s} = 200$ GeV, all of the data has stochastic cooling on. We used the data to tune a simulation for vertex distribution to see any similarities with the distribution provided from the previous Subsection 3.2.4 (Figure 3.16). The data provided contains the pattern for both particle beams, where particles are divided into bunches. In Figure 3.17 are shown bunches of particles following each other in the accelerator moving in both directions in the time interval $[0, 1000]$ ns, the Blue beam is moving towards the right, and the Yellow beam towards the left. In the image, I have selected and marked 3 bunches at the time of their overlap, more precisely a pair of opposing bunches, indexed as 1,2,3. I will present these 3 bunches here again in close-up together with their evolution.

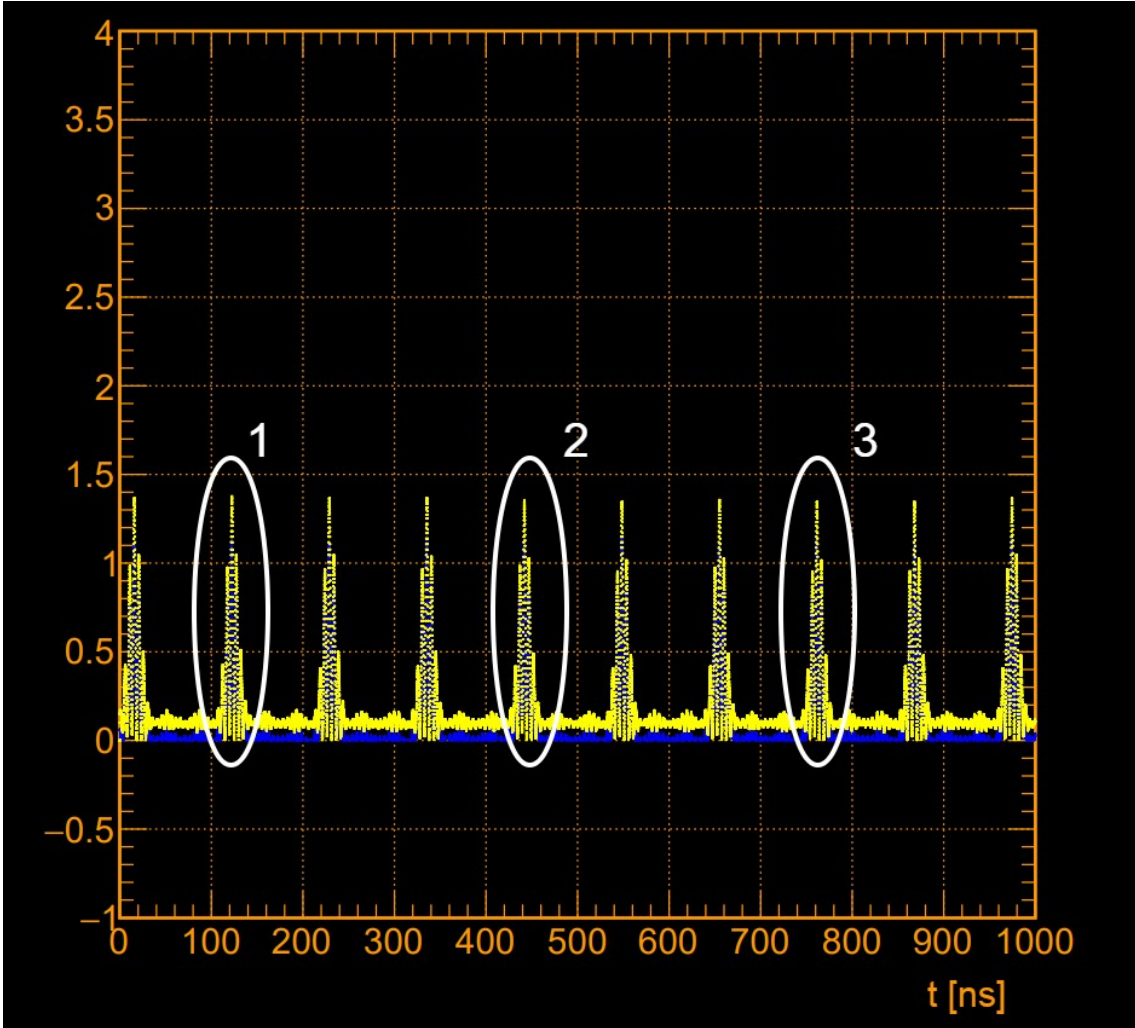


Figure 3.17: Two beams (Blue and Yellow) consisting of several bunches of particles in the collider with 3 selected bunches.

A part of the code for parameters of the bunches description is shown in Figure 3.18. The last part of the code marked with the comment `#run mode` is used for the selection of desired output.

```

86
87 #time interval for input bunches, ns
88 tmin = 0
89 tmax = 1000
90
91 #beam energy
92 Ep = 255 # GeV
93
94 #simulated particles in bunch
95 np = 30000
96
97 #emittance
98 epsilon = 20 # nm
99
100 #beta*
101 betas = 80 # cm
102
103 #space range and bins
104 nx = 60
105 xmin = -1 # mm
106 xmax = 1 # mm
107 ny = 60
108 ymin = -1 # mm
109 ymax = 1 # mm
110 #nz = 60
111 nz = 120
112 zmin = -4000 # mm
113 zmax = 4000 # mm
114
115 #time and steps for evolution
116 et0 = -15 # ns
117 et1 = 15 # ns
118 nstep = 600
119
120
121 #run mode
122 mode = "draw_input"
123 mode = "draw_xz"
124 mode = "video"
125 mode = "evolution"
126

```

Figure 3.18: Two beams (Blue and Yellow) consisting of several bunches of particles in the collider with 3 selected bunches.

I will now provide here a close-up with the predicted vertex distribution of bunches selected above from Figure 3.17. (This is a run mode `"draw_input"` and `"evolution"` in Figure 3.18.) Images of selected bunches and predicted vertex distribution, obtained by bunch evolution for a given time interval are shown below. Bunch labeled 1 in Figure 3.17 corresponding to time interval [105, 140] ns is shown in Figures 3.19 and 3.20, Bunch 2 for time interval [425, 460] ns is shown in Figures 3.21 and 3.22, and Bunch 3 for time interval [745, 780] ns is shown in Figures 3.23 and 3.24.

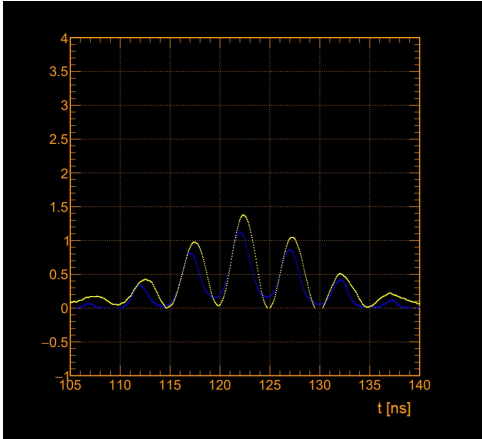


Figure 3.19: Close-up look at Bunch 1

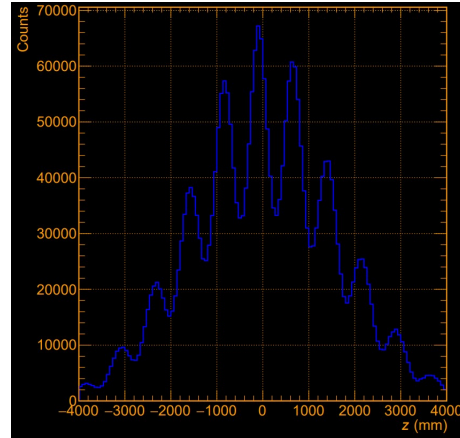


Figure 3.20: Predicted vertex distribution for Bunch 1

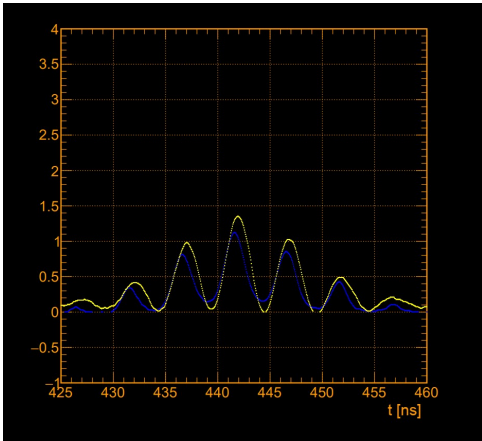


Figure 3.21: Close-up look at Bunch 2

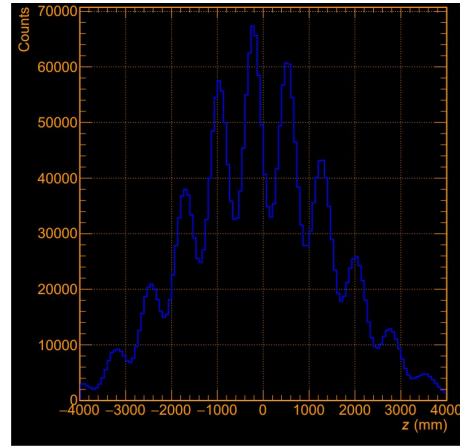


Figure 3.22: Predicted vertex distribution for Bunch 2

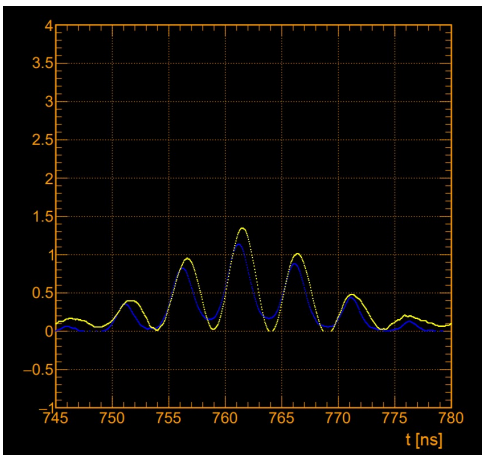


Figure 3.23: Close-up look at Bunch 3

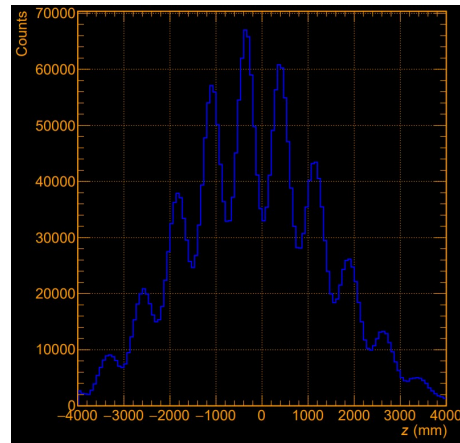


Figure 3.24: Predicted vertex distribution for Bunch 3

As in the previous cases, I will again present the parts of the code used for the creation of the images above. The program always had to be run with the set of beam parameters shown in Figure 3.18. Code for bunch rendering is shown in Figure 3.25 and for evolution in Figure 3.26.

```

66 def draw_input(lib, sim, con):
67
68     c1 = TCanvas("c1", "c1", 800, 800)
69     frame = gPad.DrawFrame(con("tmin"), -1, con("tmax"), 4) # xmin, ymin, xmax, ymax in ROOT
70
71     lib.sim_draw_input(sim)
72
73     gPad.SetGrid()
74
75     ut.invert_col(gPad)
76     c1.SaveAs("fig_input.pdf")
77

```

Figure 3.25: Code for bunch rendering in a certain time interval.

```

92 def evolution(lib, sim, con):
93
94     lib.sim_run_evolution(sim)
95
96     can = TCanvas("c1", "c1", 800, 800)
97
98     lib.sim_draw_zt(sim)
99     hzt = ut.get_obj(gPad, "hzt")
100
101     hzt.SetLineWidth(2)
102     hzt.SetLineColor(rt.kBlue)
103
104     hzt.SetXTitle("#it{z} (mm)")
105     hzt.SetYTitle("Counts")
106
107
108     ut.set_margin_lbtr(gPad, 0.15, 0.1, 0.015, 0.05)
109
110     gPad.SetGrid()
111
112     ut.invert_col(gPad)
113
114     can.SaveAs("01fig_evolution.pdf")
115

```

Figure 3.26: Code for evolution.

The final result of the simulation was a video in mp4 format for all 3 selected bunches, which, however, I cannot include in this work. I tried to replace the video with a series of images 1 ns apart that I created from this video for Bunch 1. The video shows the movement of two bunches from the given time interval [105, 140] ns and their overlap on the z-axis in time. Images of overlap shown in Figure 3.27 were taken at the same time as images shown in Figure 3.27, in which the times are displayed. Scale and axis description are shown in the last image in the sequence for both Figures 3.27 and 3.28. The order of placement of the images is in two columns, the first image is in the upper left and they go downwards. The second column contains the second half of the images.

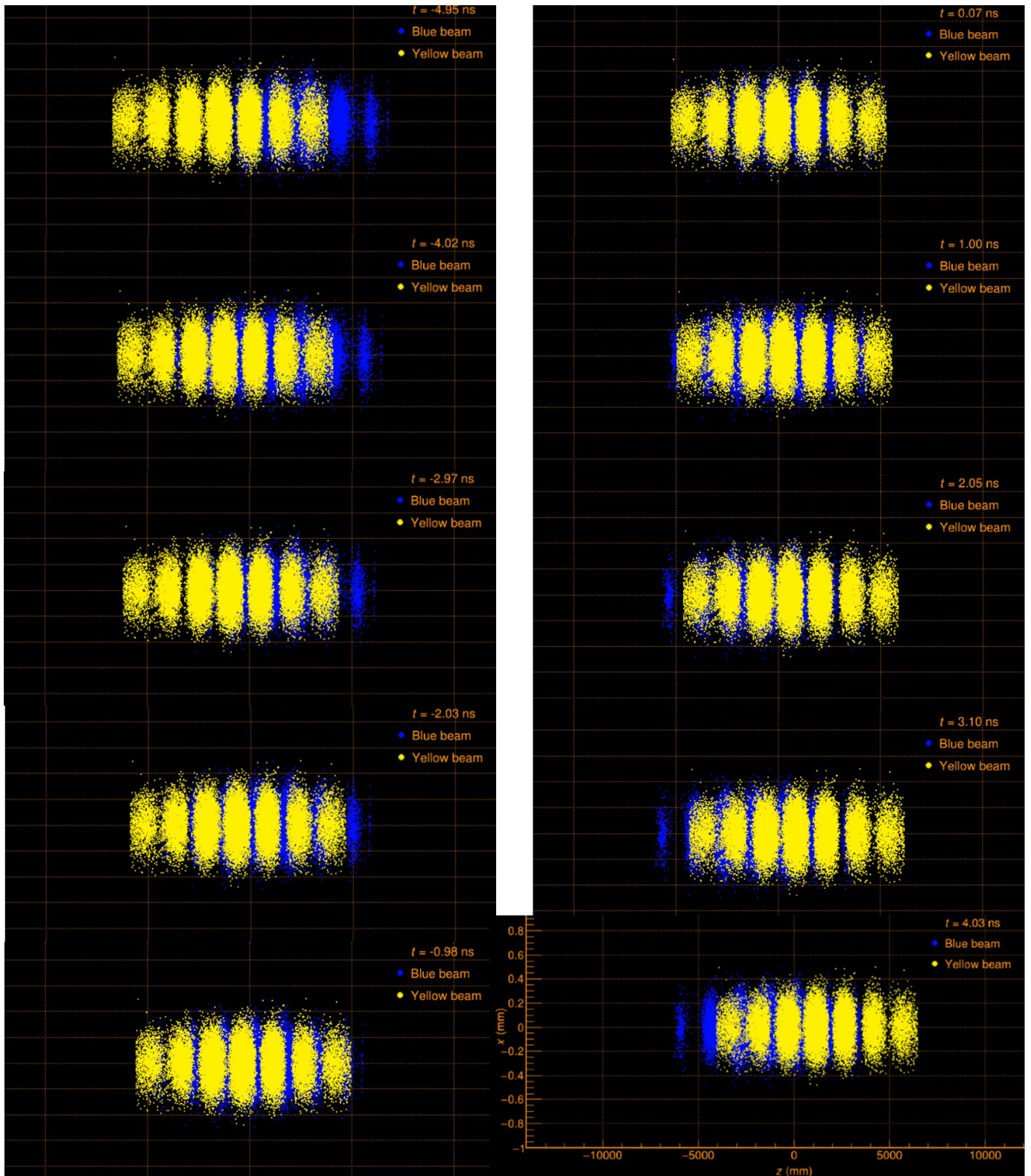


Figure 3.27: Images from video for simulation of two opposing bundles of particles collision approximately 1 ns apart covering time interval $(-5, 4)$ ns.

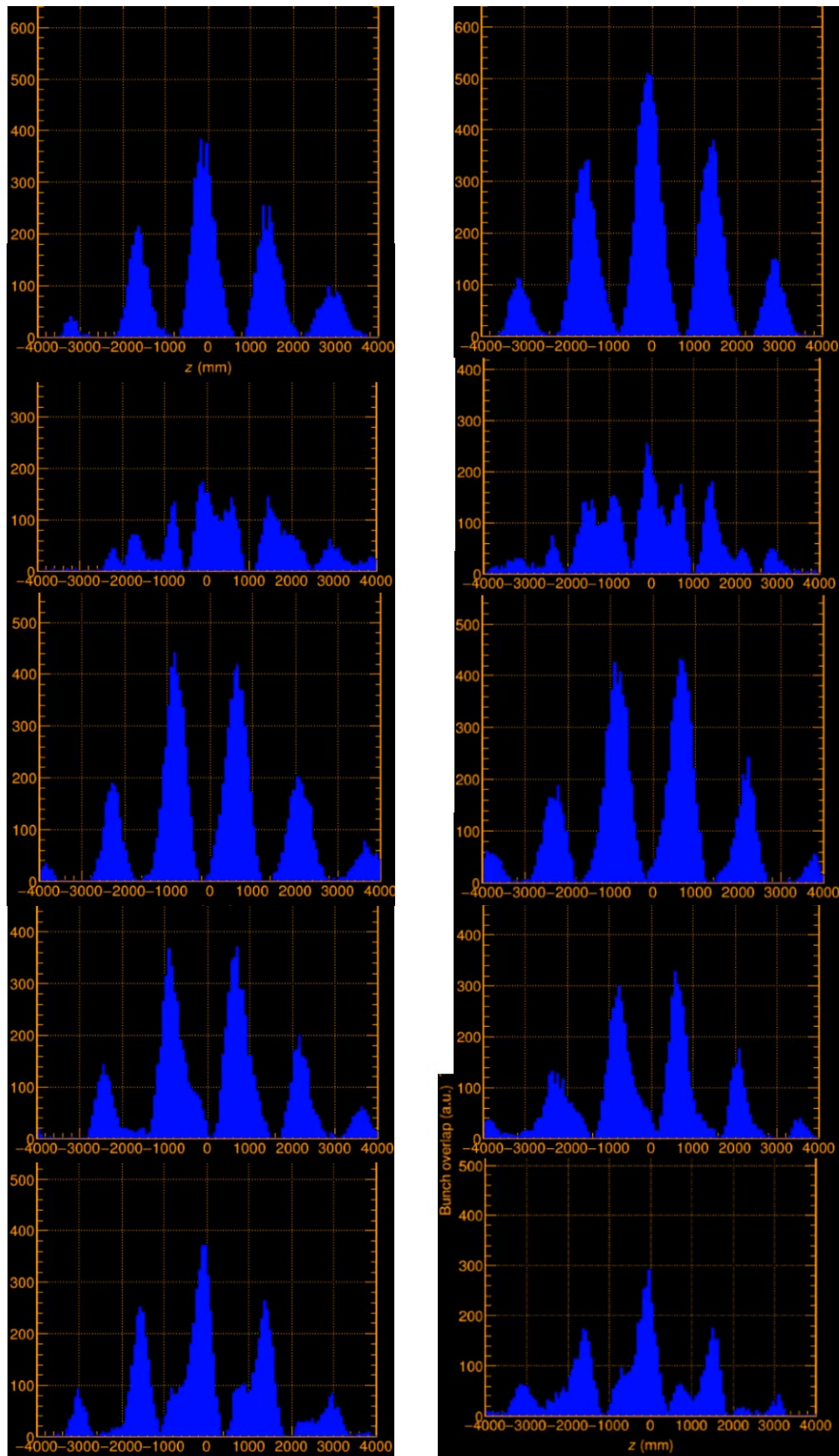


Figure 3.28: Images from video for simulation of overlap on the z -axis of two bunches in a time interval $(-5, 4)$ ns.

In the images from the video, we can see the time evolution of the movement of two opposing bunches (Figure 3.27) and the evolution of their overlap on the z-axis in time (Figure 3.28). The overlap on the z-axis is obtained by integrating the already mentioned evolution shown in Figures 3.20. I focused on tracking a specific bunch, which is labeled as 1 in Figure 3.17. From the simulation of WCM data on the fill pattern from run 14, we can observe the structure of the z-vertex distribution with peaks like on the plot provided in the previous Subsection 3.2.4 shown in Figure 3.16. Specifically, this can be seen in the evolution images (Figures 3.20, 3.22 and 3.24) or from the bunch overlap images obtained from the video of the simulation at the time of collision $t \approx 0$ (6th figure in sequence in Figure 3.28). Also, the code for loading used data and video creation is given in Appendix.

Conclusion

This thesis aimed to present the fundamental principles of ultra-peripheral collisions in heavy ion collisions. The first chapter was devoted to ultra-peripheral collisions and the basic description and classification of particles and interactions within the framework of the Standard model. In this chapter, the interactions of two colliding nuclei resulting in the photoproduction of a vector meson were described. Also, the course of the collision was described along with the possible results of such a collision. Possible theoretical predictions that the study of ultra-peripheral collisions allows were outlined, such as the gluon distribution of particles involved in the reactions.

In the next part, the Relativistic Heavy Ion Collider (RHIC) at Brookhaven National Laboratory (BNL), which makes collisions of heavy ions possible, was presented. The accelerator complex with its experiments and radio frequency system for capturing and accelerating particles was described. The main focus was on the STAR experiment, where parts of the detector were described and from which the data for the subsequent analysis originated.

In the final theoretical part, the introduction of the chapter was devoted to physical quantities used for the description of colliding particles at high energies. Subsequently, the data analysis, which is divided into three parts. For all sections, parts of code for data analysis and visualization were also provided. The first part was devoted to the observation of the J/ψ particle from its decay $J/\psi \rightarrow e^+e^-$ during Au+Au collisions at an energy $\sqrt{s} = 200$ GeV. The data for this analysis was an MC template provided by STARLIGHT, a Monte Carlo event generator from run 14. Trigger and data selection requirements were applied to the data used, which are also mentioned in this chapter. By subsequent application of restrictions on the transverse momentum, rapidity, and mass of the dielectron pair, a restriction on the area of the peak in plots and the area for coherent photoproduction of J/ψ was achieved.

The second part of the theoretical part dealt with the study of the specific structure of interaction points along the beam axis determined by forward ZDC detectors used for detecting neutrons, which are well usable in tagging UPC events. The z-vertex position data was fitted with a model of Gaussian functions and the distance between individual peaks was subsequently determined.

In the last part, the collision of two opposing beams in the accelerator was simulated. The data used for the simulation was WCM data on the fill pattern for both beams from run 14 Au+Au at $\sqrt{s} = 200$ GeV. For three selected bunches of particles, their approach and also their overlap at a certain time were displayed.

The result of the analysis was a video in mp4 format, which, however, could not be included in this work. A series of 10 images 1 ns apart is presented as a substitute for video. The simulation shows the movement of selected bunches and their overlap on the z-axis in time. The resulting structure of the overlap of bunches corresponds to the structure of interaction points along the beam axis from the previous part.

The shape of the distribution of interaction points is still an object to study. The shape of the structure presented in this thesis could be clarified by a closer study of the radio frequency system and how particles are captured and accelerated at RHIC.

Bibliography

- [1] L. Ikkanda N. Wolchover. A New Map of All the Particles and Forces. <https://www.quantamagazine.org/a-new-map-of-the-standard-model-of-particle-physics-20201022/>. Accessed: 2023-07-24.
- [2] Carlos A. Bertulani, Spencer R. Klein, and Joakim Nystrand. Physics of ultra-peripheral nuclear collisions. *Annual Review of Nuclear and Particle Science*, 55(1):271–310, 2005.
- [3] Spencer Klein and Joakim Nystrand. Ultraperipheral nuclear collisions. *Phys. Today*, 70(10):40–47, 2017.
- [4] Jaroslav Adam. Ultra-peripheral collisions in STAR. *CERN Proc.*, 1:157, 2018.
- [5] Johann Rafelski. Melting hadrons, boiling quarks. *The European Physical Journal A*, 51, 08 2015.
- [6] M. Harrison, Stephen G. Peggs, and T. Roser. The RHIC accelerator. *Ann. Rev. Nucl. Part. Sci.*, 52:425–469, 2002.
- [7] Colaboration of authors. Star detector overview. *Nuclear Instruments and Methods in Physics Research Section A: Accelerators, Spectrometers, Detectors and Associated Equipment*, 499(2):624–632, 2003. The Relativistic Heavy Ion Collider Project: RHIC and its Detectors.
- [8] STAR Colaboration. Proposal for a Large Area Time of Flight System for STAR. <https://www.star.bnl.gov/public/tof/>. Accessed: 2023-07-20.
- [9] Frank Geurts. Dielectron measurements in star. *EPJ Web of Conferences*, 36, 08 2012.
- [10] T.M Cormier, A.I Pavlinov, M.V Rykov, V.L Rykov, and K.E Shestermanov. Star barrel electromagnetic calorimeter absolute calibration using “minimum ionizing particles” from collisions at rhic. *Nuclear Instruments and Methods in Physics Research Section A: Accelerators, Spectrometers, Detectors and Associated Equipment*, 483(3):734–746, 2002.
- [11] Yi-Fei Xu, Jin-Hui Chen, Yu-Gang Ma, Ai-Hong Tang, Zhang-Bu Xu, and Yu-Hui Zhu. Physics performance of the STAR zero degree calorimeter at relativistic heavy ion collider. *Nucl. Sci. Tech.*, 27(6):126, 2016.

- [12] The STAR Forward Calorimeter System and Forward Tracking System. <https://drupal.star.bnl.gov/STAR/files/ForwardUpgrade.v20.pdf>.
- [13] J. Čepila. *Subatomová fyzika - studijní skriptum*. 2021.
- [14] V. Petráček. *Subatomová fyzika I*. 2009.
- [15] Robert Mann. *An Introduction to Particle Physics and the Standard Model*. Taylor & Francis, 2010.
- [16] R. L. Workman et al. Review of Particle Physics. *PTEP*, 2022:083C01, 2022.
- [17] S. Timoshenko. Ultra-peripheral heavy ion collisions at STAR. *Conf. Proc. C*, 060726:414–417, 2006.
- [18] J. G. Contreras and J. D. Tapia Takaki. Ultra-peripheral heavy-ion collisions at the LHC. *Int. J. Mod. Phys. A*, 30:1542012, 2015.
- [19] Peter A. Steinberg. Ultraperipheral Collisions at RHIC and the LHC. *Nucl. Phys. A*, 1005:122007, 2021.
- [20] Tsunehiro Kobayashi. High Energy Photo-Reactions and Generalized Vector Meson Dominance Model in the Relativistically Extended Quark Model. *Progress of Theoretical Physics*, 49(1):282–292, 01 1973.
- [21] Robert P. Crease. Recombinant science: The birth of the relativistic heavy ion collider (rhic). *Historical Studies in the Natural Sciences*, 38(4):535–568, 2008.
- [22] Robert P. Crease and Robert W. Seidel. Making Physics: A Biography of Brookhaven National Laboratory, 1946–1972. *Physics Today*, 53(1):55–55, 01 2000.
- [23] Brookheaven National Laboratory, Relativistic Heavy Ion Collider. <https://www.bnl.gov/rhic/>. Accessed: 2023-07-20.
- [24] Kevin Brown, Leif Ahrens, I Hung Chiang, Christopher Gardner, David Gassner, Lee Hammons, Margaret Harvey, Nicholas Kling, John Morris, Phillip Pile, Adam Rusek, Mike Sivertz, Dannie Steski, Nick Tsoupas, and Keith Zeno. The nasa space radiation laboratory at brookhaven national laboratory: Preparation and delivery of ion beams for space radiation research. *Nuclear Instruments and Methods in Physics Research Section A: Accelerators, Spectrometers, Detectors and Associated Equipment*, 618(1):97–107, 2010.
- [25] Brookheaven National Laboratory, Relativistic Heavy Ion Collider. <https://www.bnl.gov/nsls2/research/>. Accessed: 2023-07-20.
- [26] M. Harrison, T. Ludlam, and S. Ozaki. Rhic project overview. *Nuclear Instruments and Methods in Physics Research Section A: Accelerators, Spectrometers, Detectors and Associated Equipment*, 499(2):235–244, 2003. The Relativistic Heavy Ion Collider Project: RHIC and its Detectors.

- [27] H. Hahn, E. Forsyth, H. Foelsche, M. Harrison, J. Kewisch, G. Parzen, S. Peggs, E. Raka, A. Ruggiero, A. Stevens, S. Tepikian, P. Thieberger, D. Trbojevic, J. Wei, E. Willen, S. Ozaki, and S.Y. Lee. The rhic design overview. *Nuclear Instruments and Methods in Physics Research Section A: Accelerators, Spectrometers, Detectors and Associated Equipment*, 499(2):245–263, 2003. The Relativistic Heavy Ion Collider Project: RHIC and its Detectors.
- [28] Alexander Wu Chao, Karl Hubert Mess, Maury Tigner, and Frank Zimmermann, editors. *Handbook of accelerator physics and engineering: 2nd Edition*. World Scientific, Hackensack, USA, 2 edition, 2013.
- [29] S. Y. Lee. *Accelerator physics*. 1999.
- [30] Collaboration of authors. The brahms experiment at rhic. *Nuclear Instruments and Methods in Physics Research Section A: Accelerators, Spectrometers, Detectors and Associated Equipment*, 499(2):437–468, 2003. The Relativistic Heavy Ion Collider Project: RHIC and its Detectors.
- [31] Collaboration of authors. The phobos detector at rhic. *Nuclear Instruments and Methods in Physics Research Section A: Accelerators, Spectrometers, Detectors and Associated Equipment*, 499(2):603–623, 2003. The Relativistic Heavy Ion Collider Project: RHIC and its Detectors.
- [32] Collaboration of authors. Phenix detector overview. *Nuclear Instruments and Methods in Physics Research Section A: Accelerators, Spectrometers, Detectors and Associated Equipment*, 499(2):469–479, 2003. The Relativistic Heavy Ion Collider Project: RHIC and its Detectors.
- [33] Takao Sakaguchi. sPHENIX overview. https://indico.cern.ch/event/827540/contributions/3463452/attachments/1878444/3094012/sPHENIX_overview_final.pdf.
- [34] Brookhaven National Laboratory, Relativistic Heavy Ion Collider. <https://www.bnl.gov/rhic/sphenix.php/>. Accessed: 2023-07-20.
- [35] R.L. Brown, Asher Etkin, K.J. Foley, W.J. Leonhardt, J.A. Mills, I. Polk, E.S. Rodger, J.A. Scheblein, and R.D. Schlueter. The star detector magnet subsystem. volume 3, pages 3230 – 3232 vol.3, 06 1997.
- [36] Collaboration of authors. The STAR time projection chamber: a unique tool for studying high multiplicity events at RHIC. *Nuclear Instruments and Methods in Physics Research Section A: Accelerators, Spectrometers, Detectors and Associated Equipment*, 499(2-3):659–678, mar 2003.
- [37] B Lasiuk, Yu Andrés, André Braem, D Cozza, Martyn Davenport, G Cataldo, L Dell’Olio, Domenico Di Bari, Antonio Di Mauro, J. Dunlop, Evan Finch, Daniel Fraissard, A. Franco, Jenifer Gans, B Ghidini, John Harris, Matt Horsley, Gerd Kunde, Y. Lesenechal, and Z Xu. The star-rich detector. 698, 02 2002.

-
- [38] C. E. Allgower et al. The STAR endcap electromagnetic calorimeter. *Nucl. Instrum. Meth. A*, 499:740–750, 2003.
- [39] C. Whitten. The beam-beam counter: A local polarimeter at star. 980, 02 2008.
- [40] Joseph Adams et al. The STAR Event Plane Detector. *Nucl. Instrum. Meth. A*, 968:163970, 2020.
- [41] T. C. Huang et al. Muon Identification with Muon Telescope Detector at the STAR Experiment. *Nucl. Instrum. Meth. A*, 833:88–93, 2016.
- [42] W. J. Llope et al. The STAR Vertex Position Detector. *Nucl. Instrum. Meth. A*, 759:23–28, 2014.
- [43] Collaboration of authors. Phenix calorimeter. *Nuclear Instruments and Methods in Physics Research Section A: Accelerators, Spectrometers, Detectors and Associated Equipment*, 499(2):521–536, 2003. The Relativistic Heavy Ion Collider Project: RHIC and its Detectors.
- [44] STARlight. <https://starlight.hepforge.org/>. Accessed: 2023-07-24.
- [45] M. Broz, J.G. Contreras, and J.D. Tapia Takaki. A generator of forward neutrons for ultra-peripheral collisions: noon. *Computer Physics Communications*, 253:107181, 2020.
- [46] Sunrise. <https://nms.fjfi.cvut.cz/wiki/Sunrise.fjfi.cvut.cz>. Accessed: 2023-07-24.
- [47] BNL W. Schmidke. Ultra-Peripheral Collisions at STAR. https://indico.cern.ch/event/782953/contributions/3455005/attachments/1887083/3111226/STAR_UPC.pdf. Accessed: 2023-07-24.
- [48] Jaroslav Adam. Coherent J/ψ photoproduction in ultra-peripheral collisions at STAR. *PoS, DIS2019:042*, 2019.

Appendix

Part of the code used for video creation

```
1 #!/cvmfs/sft.cern.ch/lcg/views/LCG_98python3/x86_64-centos7-gcc8-opt/bin/python3
2
3
4 import sys
5 from ctypes import CDLL, c_char_p, c_double, c_void_p
6 import os
7
8 import ROOT as rt
9 from ROOT import gPad, gROOT, gStyle, gSystem, TCanvas, TH1D
10 from ROOT import TIter
11
12 sys.path.append("./python")
13 import plot_utils as ut
14 from read_con import read_con
15
16 #-----
17 def main():
18
19     #configuration from command line
20     config = get_config()
21     con = read_con(config)
22
23     #analysis library
24     lib = CDLL("build/librhc_beam_shape.so")
25
26     #simulation instance
27     lib.make_sim.restype = c_void_p
28     sim = c_void_p( lib.make_sim( c_char_p(bytes(config, "utf-8")) ) )
29
30     print(con.str("mode"))
31
32     #functions
33     func = {}
34     func["evolution"] = evolution
35     func["video"] = video
36     func["draw_xz"] = draw_xz
37     func["draw_input"] = draw_input
38
39     #call the function selected in the configuration
40     func[con.str("mode")](lib, sim, con)
```

Figure 3.29: Code for loading the data and functions for output.

```
105 def video(lib, sim, con):
106
107     #ns
108     tmin = con.flt("tmin", "video")
109     tmax = con.flt("tmax", "video")
110     nstep = con.int("nstep", "video")
111
112     dt = float(tmax-tmin)/nstep
113     time = tmin-dt
114     lib.sim_move(sim, c_double(time))
115
116     can = TCanvas("c1", "c1", 950, 950)
117
118     #temporary directory
119     #os.system("rm -f "+out)
120     os.system("rm -rf tmp")
121     os.system("mkdir tmp")
122
123     for i in range(nstep):
124
125         lib.sim_move(sim, c_double(dt))
126
127         time += dt
128         can.Clear()
129
130         nam = "tmp/fig_"+"{0:04d}".format(i)+".png"
131         create_plot_pairs(lib, sim, can, nam, time)#, cross_angle, can, zpmx, time, nam)
132
133     #command to make the video
134     os.system(con.str("cmd", "video"))
135
136     #remove the temporary directory
137     os.system("rm -rf tmp")
138
```

Figure 3.30: Code for video creation.